PHYSICAL REVIEW B **104**, 174204 (2021)

Editors' Suggestion

# Collective dynamics of liquid deuterium: Neutron scattering and approximate quantum simulation methods

Eleonora Guarini,[1,*] Fabrizio Barocchi,[1] Alessio De Francesco,[2] Ferdinando Formisano,[2] Alessio Laloni,[3] Ubaldo Bafile,[4] Milva Celli,[4] Daniele Colognesi,[4] Renato Magli,[5] Alessandro Cunsolo,[6] and Martin Neumann[7]

[1]*Dipartimento di Fisica e Astronomia, Università degli Studi di Firenze, via G. Sansone 1, I-50019 Sesto Fiorentino, Italy*
[2]*CNR-IOM & INSIDE@ILL c/o Operative Group in Grenoble (OGG) F-38042 Grenoble, France*
*and Institut Laue Langevin (ILL) F-38042 Grenoble, France*
[3]*CNR-IOM & INSIDE@ILL c/o Operative Group in Grenoble (OGG) F-38042 Grenoble, France*
*and European Spallation Source ERIC, P.O. Box 176, SE-221 Lund, Sweden*
[4]*Consiglio Nazionale delle Ricerche, Istituto di Fisica Applicata "Nello Carrara", via Madonna del Piano 10, I-50019 Sesto Fiorentino, Italy*
[5]*Dipartimento di Scienze Biomediche, Chirurgiche ed Odontoiatriche, Università di Milano Statale, via Saldini 50, I-20133 Milano, Italy*
[6]*Department of Physics, University of Wisconsin at Madison, 1150 University Avenue, Madison, Wisconsin, USA*
[7]*Fakultät für Physik der Universität Wien, Kolingasse 14-16, A-1090 Wien, Austria*

(Received 5 September 2021; revised 25 October 2021; accepted 28 October 2021; published 10 November 2021)

We present an experimental and simulation study of the collective dynamics of liquid $D_2$ in the range of exchanged wave vectors $3 \leqslant Q \leqslant 14\ \mathrm{nm}^{-1}$. Neutron Brillouin scattering results for the center-of-mass dynamic structure factor of this moderately quantum fluid are compared, on an absolute scale, with those obtained by three different quantum simulation methods such as ring polymer molecular dynamics and two versions of the Feynman-Kleinert approach. The experimental data can be well described by dynamical models typically used for liquids. Some discrepancies show up both among simulations, and between simulations and experimental data. Such discrepancies are found to mainly concern the damping of the propagating sound modes.

DOI: 10.1103/PhysRevB.104.174204

## I. INTRODUCTION

Cryogenic fluids have always attracted much interest, owing to both fundamental and technical reasons. In particular, the hydrogen liquids (mainly $H_2$ and $D_2$) display a weakly quantum behavior (see e.g., Ref. [1] for a brief description) still challenging simulation-based determinations of their dynamical properties and, at the same time, are the most used moderating materials for the production of cold neutrons (i.e., with energies around 1 meV), which are quite important spectroscopic probes in condensed matter research. From such an applicative point of view, a good knowledge of the neutron double differential cross sections (DDCS) of $H_2$, $D_2$, and other moderating materials has become an indispensable requirement for a proper development and operation of neutron sources.

The neutron DDCS depends in an essential way on both the collective and the single-particle dynamics, embodied by the total $S(Q,\omega)$, and *self* (single-particle) $S_s(Q,\omega)$ center-of-mass dynamic structure factors, respectively. Unfortunately, in these liquids, the former is far from being well known. This fact constitutes a problem particularly for $D_2$ where, differently from $H_2$, the *distinct* (interparticle) and the single-particle dynamics [2,3] are almost equally relevant, being the incoherent and coherent scattering nuclear cross sections of comparable magnitudes for the deuteron [4].

An appropriate design of new-generation $D_2$-based cold neutron sources, therefore, crucially depends on researchers‘ ability in computing both the coherent and incoherent components contributing to the DDCS of this molecular system in its liquid phase. This implies that future progress in this field is also intimately tied to the development of reliable simulation methods permitting to build up the extended $S(Q,\omega)$ databases needed in such applications, and which of course it is hard to try to collect by means of demanding and time-consuming experiments.

However, the effects of particle quantum delocalization in this low mass and low temperature liquid, which have for long been neglected in nuclear data processing [5,6] and in the past attempts to model its DDCS [7–9], make the (clearly convenient) simulation route quite a demanding task, as well. As mentioned, this is particularly true in the $D_2$ case, since a good prediction of the total $S(Q,\omega)$ is as important as that of its self part alone, namely $S_s(Q,\omega)$. Concerning the latter, we showed a few years ago [10,11] that present quantum simulation methods like Centroid Molecular Dynamics (CMD) [12–15] and Ring Polymer Molecular Dynamics (RPMD) [16–18], used in combination with the isotropic Silvera-Goldman pair potential [19], provide good estimates of the velocity autocorrelation function of the hydrogen liquids. Therefore, by means of the Gaussian approximation [20,21], it is possible to obtain quite reliable, quantum compliant, determinations of the center-of-mass $S_s(Q,\omega)$ of both $H_2$ and $D_2$. In fact, through this method, a quite good agreement with experimental total cross-section data was found for both $H_2$ and $D_2$ in the respective incident

---

[*] Corresponding author: guarini@fi.infn.it

energy ranges where the contribution of the distinct part of $S(Q,\omega)$ turns out to be negligible (see e.g., Figs. 12 and 14 of Ref. [22]).

The situation is instead far less defined as soon as one considers the *direct* simulation of both $S(Q,\omega)$ and $S_s(Q,\omega)$ by quantum techniques, since two problems exist. The first depends on the fact that the autocorrelation of the Fourier components of density fluctuations contains position operators in exponential form, and such a nonlinearity represents an intrinsic limitation, difficult to deal with, of both the CMD and RPMD schematizations [13,16,18]. The second is related to the form in which both neutron [23–28] and x-ray [29] inelastic scattering data on $D_2$ have been published, which strongly hinders reliable comparisons with simulation results for the center-of-mass dynamics. In both experimental cases the results are indeed only given in arbitrary units and within the instrumental finite resolution of each specific measurement. Moreover, in the specific case of neutron scattering, only the DDCS spectra have been reported with no attempt to extract the coherent component, i.e., the key quantity $S(Q,\omega)$, from the total signal. In other words, the center-of-mass dynamic structure factor of liquid $D_2$ in absolute units and free from resolution effects has never been published, despite the various neutron scattering experiments devoted to this sample in the 1990s [23–27] and in more recent years [28].

This serious lack is partly the cause, in our view, of the still confused picture we have about the performance of quantum simulation algorithms for direct determinations of the dynamic structure factors. The only, rather recent, exceptions in the literature regard (i) the performance of the Feynman-Kleinert Linearized Path Integral (FK-LPI) method [30], which was tested against a revised analysis [31] of the quoted x-ray data [29], and (ii) a similar comparison [32] carried out to evaluate the accuracy of the Feynman-Kleinert Quasi Classical Wigner (FK-QCW) modification [33] of the previous FK-LPI algorithm. Clearly, these last works [31,32] have the great merit to finally explore the level of agreement between quantum simulations and experimental results for $S(Q,\omega)$. Regretfully, it is not easy to catch the details of the comparisons from the published figures. Moreover, the x-ray data there reported were not fully independent of the simulations since, as explained by the authors, the latter were used, either in the FK-LPI or in the FK-QCW form, to refine the extraction of $S(Q,\omega)$ from the raw x-ray spectra. A further limitation concerns the missing normalization of $S(Q,\omega)$ to absolute units and its resolution broadening. Especially when quantitative comparisons cannot be relaxed, as it is the case of real applications, agreements regarding only an unnormalized broadened spectral shape are obviously insufficient.

What we described above is the background motivating our present work on the dynamics of liquid $D_2$, with which we try to achieve four goals: (i) to provide an absolute scale determination of its neutron DDCS that might serve as a reference in tests of the computations for cold source design and total cross-section calculations; (ii) to derive $S(Q,\omega)$ in absolute units in a $Q$ range, which is significant for studies of the collective dynamics [i.e., from a few inverse nanometers up to wave vectors larger than $Q_p/2$, with $Q_p$ being the position of the main maximum in the static structure factor $S(Q)$]; (iii) to analyze the relaxation and excitation modes of the fluid; and (iv) to compare the experimental $S(Q,\omega)$ with the one obtained from RPMD, FK-LPI, FK-QCW simulations.

The lineshape analysis of the neutron data carried out by using the Lorentzian modes decomposition introduced some years ago [34–36] ensures that (at least) the lower-order spectral moments predicted for a quantum system are satisfied [21]. Therefore, we present an experimental study of the collective dynamics conducted with the highest possible control on the physical consistency of the results and on their compliance with fundamental properties of the dynamic structure factor of a quantum fluid. We will show that previous analyses, performed without imposing physical constraints in the fit procedure, led to quite different results whose reliability is therefore rather uncertain.

Before describing the experiment and the analysis of the neutron data, it is useful to review the formal apparatus providing an expression for the neutron DDCS of a homonuclear diatomic low-temperature liquid, and of $D_2$ in particular. In the next section we summarize the basic formulas enabling the treatment of the response to an unpolarized neutron beam of such a molecular fluid, in its *normal* (67% *ortho* – 33% *para*) composition, assuming that its molecules behave as freely rotating harmonic oscillators, i.e., their interaction is governed by an isotropic intermolecular potential, with translations completely decoupled from the intramolecular degrees of freedom.

## II. GENERAL FORMALISM FOR THE DDCS OF LIQUID $D_2$

The property of a molecular system, which is probed by neutron scattering [37,38] (denoted by the subscript "n") is the combination

$$F_n(Q,t) = u(Q)F(Q,t) + [v(Q,t) - u(Q)]F_s(Q,t), \tag{1}$$

of the center-of-mass total and single-molecule (or self) intermediate scattering functions, defined, respectively, as

$$F(Q,t) = \frac{1}{N}\sum_{i,j=1}^{N}\langle e^{-i\boldsymbol{Q}\cdot\boldsymbol{r}_i(0)}e^{i\boldsymbol{Q}\cdot\boldsymbol{r}_j(t)}\rangle, \tag{2}$$

$$F_s(Q,t) = \frac{1}{N}\sum_{i=1}^{N}\langle e^{-i\boldsymbol{Q}\cdot\boldsymbol{r}_i(0)}e^{i\boldsymbol{Q}\cdot\boldsymbol{r}_i(t)}\rangle \tag{3}$$

with $\boldsymbol{r}_j(t)$ denoting the position vector of the center of mass of the $j$th molecule at a generic time $t$, $N$ being the total number of molecules in the system. The right-hand side of Eqs. (2) and (3) are the autocorrelation functions of the Fourier components, with wave vector $\boldsymbol{Q}$, of the microscopic density [2], which, except for purely classical systems, are in general complex quantities. In Eq. (1), the functions $u(Q)$ and $v(Q,t) - u(Q)$ are the molecular equivalents, respectively, of $b_{\mathrm{coh}}^2$ and $b_{\mathrm{inc}}^2$ in the monatomic case, where $b_{\mathrm{coh}}$ and $b_{\mathrm{inc}}$ are the coherent and incoherent neutron scattering lengths of the nuclear species. Following the general treatment of homonuclear diatomic molecules proposed by Young and Koppel in 1964 [39], it is possible to obtain expressions for $u(Q)$ and $v(Q,t)$ that depend on the scattering lengths, the initial state probabilities, the rotovibrational quantum numbers, and the nuclear spin statistics [38]. In particular $v(Q,t)$, which also depends on the ortho-para concentration, contains combinations of the coherent and incoherent scattering lengths, which have different expressions (see Table II of Ref. [38]) according to whether the nuclei of the molecule are bosons or fermions. This implies that, when expressing $v(Q,t)$ in the general form [38]

$$v(Q,t) = \sum_{J_0 J_1 v_0 v_1} e^{i\omega_{J_0J_1}t} e^{i\omega_{v_0v_1}t} \mathcal{F}(Q; J_0, J_1, v_0, v_1), \tag{4}$$

the function $\mathcal{F}(Q; J_0, J_1, v_0, v_1)$ changes when passing from $H_2$ to $D_2$, in addition, of course, to its variations related to the specific transition, sample composition, and thermodynamic conditions. In Eq. (4), the rotational ($\omega_{J_0J_1}$) and vibrational ($\omega_{v_0v_1}$) transition frequencies, involving the initial (subscript 0) and final (subscript 1) quantum numbers, are seen to determine the time dependence of $v(Q,t)$. In the special case of a low-temperature sample, all molecules are assumed to lie initially in the vibrational ground state ($v_0 = 0$), therefore it is possible to write $\omega_{v_0v_1} = v_1\omega_{\rm v}$, with $\omega_{\rm v}$ indicating the frequency of the harmonic oscillator of reduced mass $\mu = M/4$ in the homonuclear diatomic case ($M$ is the total molecular mass). It is important to underline that, differently from $v(Q,t)$, which depends on both the coherent and incoherent scattering lengths, $u(Q)$ contains only the coherent one.

By performing the time Fourier transform of Eq. (1), one can also write the neutron version of the dynamic structure factor as

$$\begin{aligned} S_{\rm n}(Q,\omega) &= \frac{1}{2\pi}\left\{u(Q)\int_{-\infty}^{+\infty} dt\, e^{-i\omega t} F(Q,t) + \int_{-\infty}^{+\infty} dt\, e^{-i\omega t}[v(Q,t) - u(Q)]F_{\rm s}(Q,t)\right\} \\ &= u(Q)S(Q,\omega) + J_{\rm s}(Q,\omega), \end{aligned} \tag{5}$$

where, using Eqs. (1) and (4) with $v_0 = 0$, $J_{\rm s}(Q,\omega)$ is given by

$$\begin{aligned} J_{\rm s}(Q,\omega) &= \left[\frac{1}{2\pi}\int_{-\infty}^{+\infty} dt\, e^{-i\omega t} v(Q,t) F_{\rm s}(Q,t)\right] - u(Q)S_{\rm s}(Q,\omega) \\ &= \frac{1}{2\pi}\sum_{J_0J_1v_1}\int_{-\infty}^{+\infty} dt\, e^{-i(\omega-\omega_{J_0J_1}-v_1\omega_{\rm v})t}\mathcal{F}(Q; J_0, J_1, 0, v_1)F_{\rm s}(Q,t) - u(Q)S_{\rm s}(Q,\omega) \\ &= \sum_{J_0J_1v_1}\mathcal{F}(Q; J_0, J_1, 0, v_1)S_{\rm s}(Q, \omega - \omega_{J_0J_1} - v_1\omega_{\rm v}) - u(Q)S_{\rm s}(Q,\omega). \end{aligned} \tag{6}$$

Details for the calculation of $u(Q)$ and $\mathcal{F}(Q; J_0, J_1, v_0, v_1)$ can be found in Ref. [38].

The first term in Eq. (5) is therefore related to the center-of-mass total dynamic structure factor $S(Q,\omega)$ we are interested in when studying the translational collective dynamics of the system. The second term $J_{\rm s}(Q,\omega)$ is instead related, in the way shown in Eq. (6), to the single-molecule translational dynamics expressed by $S_{\rm s}(Q,\omega)$, and plays the same role that incoherent scattering plays in the monatomic case. Therefore, such a contribution must be duly evaluated, and then subtracted from the neutron signal. In particular, the first term in the last row of Eq. (6) is seen to correspond to a comb of lines centered at the frequencies of the possible rotovibrational transitions. These spectral components are therefore either central or shifted replicas of the lineshape describing the center-of-mass $S_{\rm s}(Q,\omega)$, with amplitudes ruled, as mentioned, by the involved quantum numbers, the initial state probabilities and the nuclear scattering lengths. Consequently, the DDCS of a homonuclear diatomic liquid can be straightforwardly obtained from the previous equations according to the general definition

$$\frac{\partial^2\sigma}{\partial\Omega\partial\omega} = \frac{k_1}{k_0}S_{\rm n}(Q,\omega), \tag{7}$$

where $k_0$ and $k_1$ are the moduli of the incident and scattered neutron wave vectors.

It is important to recall that the spectra $S(Q,\omega)$ and $S_{\rm s}(Q,\omega)$ of the complex-valued standard quantum intermediate scattering functions $F(Q,t)$ and $F_{\rm s}(Q,t)$ obey the detailed balance principle, that is

$$S(Q,\omega) = e^{\beta\hbar\omega}S(Q,-\omega), \tag{8}$$

where $\hbar = h/(2\pi)$ is the reduced Planck constant and $\beta = (k_{\rm B}T)^{-1}$, with $k_{\rm B}$ the Boltzmann constant and $T$ the temperature of the fluid. An analogous equality holds for $S_{\rm s}(Q,\omega)$. Therefore, they are asymmetric functions of $\omega$ with a nonzero first spectral moment given by [21]

$$M^{(1)} = \int_{-\infty}^{+\infty} d\omega\,\omega\, S(Q,\omega) = \frac{\hbar Q^2}{2M} = \omega_{\rm r}, \tag{9}$$

and the same holds for $S_{\rm s}(Q,\omega)$, i.e., both moments are given by the recoil frequency $\omega_{\rm r}$. Similarly, the second frequency moment is different from the classical value $Q^2/(M\beta)$ and, for $S_{\rm s}(Q,\omega)$, takes the form [21]

$$M_{\rm s}^{(2)} = \int_{-\infty}^{+\infty} d\omega\,\omega^2\, S_{\rm s}(Q,\omega) = \omega_{\rm r}^2 + \frac{2Q^2}{3M}\langle E_{\rm K}\rangle, \tag{10}$$

where $\langle E_{\rm K}\rangle$ is the mean translational kinetic energy, which in these low-mass and low-temperature fluids differs considerably [1] from the classical value $3/(2\beta)$, as can be found, for instance, by means of path-integral Monte Carlo (PIMC) simulations [40]. The expression for the second frequency moment of $S(Q,\omega)$ is more complex, as can be verified from Eq. (35) of Ref. [21] to which we direct the reader for details.

Scattering experiments actually provide the "true" quantum spectra discussed above, although within the finite-energy resolution of the used instrument. Conversely, as far as quantum simulations are concerned, two of the quoted methods, i.e., RPMD and CMD, do not directly give the quantum autocorrelations, but the so-called *canonical* or Kubo-transformed [41] ones, which in the case of the intermediate scattering function is defined by

$$F_{\mathrm{K}}(Q,t)=\frac{1}{N}\sum_{i,j=1}^{N}\frac{1}{\beta}\int_0^\beta d\lambda\,\langle e^{\lambda H}e^{-i\boldsymbol{Q}\cdot\boldsymbol{r}_i(0)}e^{-\lambda H}e^{i\boldsymbol{Q}\cdot\boldsymbol{r}_j(t)}\rangle, \tag{11}$$

where $H$ is the Hamiltonian operator of the system. A similar expression can be written for the self function $F_{\mathrm{s,K}}(Q,t)$. Equation (11) represents an even and real-valued quantity, whose $t=0$ value, denoted as $S_{\mathrm{K}}(Q)$, is not the "true" static structure factor $S(Q)$ measured by diffraction experiments. In an analogous way, we will use the notation $S_{\mathrm{K}}(Q,\omega)$ for the spectrum of Eq. (11), and a similar one for the corresponding single-molecule function.

The important properties of Kubo spectra are that these are (more manageable) symmetric functions of $\omega$, which can be shown, via the fluctuation-dissipation theorem [41], to be related, in the frequency domain, to the genuine quantum spectra through

$$S(Q,\omega)=\frac{\beta\hbar\omega}{1-e^{-\beta\hbar\omega}}S_{\mathrm{K}}(Q,\omega), \tag{12}$$

and again a similar expression holds for the self case. Concerning the spectral moments of $S_{\mathrm{K}}(Q,\omega)$, of course the first one $M_{\mathrm{K}}^{(1)}$ is zero, while the second $M_{\mathrm{K}}^{(2)}$ coincides, also for the single-particle spectrum, with the classical value quoted before. Note that a useful relation [3] links the even moments of the Kubo spectrum $M_{\mathrm{K}}^{(2k)}$ to the odd ones of the quantum spectrum $M^{(2k-1)}$, with $k=1,2,\dots$. In particular, for $k=1$, one has

$$M_{\mathrm{K}}^{(2)}=\frac{Q^2}{M\beta}=\frac{2}{\hbar\beta}\omega_{\mathrm{r}}=\frac{2}{\hbar\beta}M^{(1)}. \tag{13}$$

Therefore, while fitting to experimental data the model function described later in Sec. IV, which contains some model of $S_{\mathrm{K}}(Q,\omega)$ and uses Eq. (12) to derive a model $S(Q,\omega)$, the enforcement of the second moment sum rule for $S_{\mathrm{K}}(Q,\omega)$ corresponds to doing the same at the level of the first-frequency moment of the fitted $S(Q,\omega)$.

Since $S(Q,\omega)$ (and $S_{\mathrm{s}}(Q,\omega)$) can be split into symmetric (subscript sym) and antisymmetric (subscript antisym) frequency contributions, according to

$$\begin{aligned}S(Q,\omega)&=S_{\mathrm{sym}}(Q,\omega)+S_{\mathrm{antisym}}(Q,\omega)\\&=\frac{1}{2\pi}\int_{-\infty}^{+\infty}dt\,[\mathrm{Re}F(Q,t)\cos(\omega t)\\&\quad+\mathrm{Im}F(Q,t)\sin(\omega t)],\end{aligned} \tag{14}$$

it is also possible to verify that the Kubo spectrum is linked to the quantum antisymmetric and symmetric components of $S(Q,\omega)$ in the following way [21]:

$$S_{\mathrm{K}}(Q,\omega)=\frac{\tanh(\beta\hbar\omega/2)}{\beta\hbar\omega/2}S_{\mathrm{sym}}(Q,\omega)=\frac{1}{\beta\hbar\omega/2}S_{\mathrm{antisym}}(Q,\omega), \tag{15}$$

which also gives the relation between $S_{\mathrm{sym}}(Q,\omega)$ and $S_{\mathrm{antisym}}(Q,\omega)$ that can be used, together with Eq. (14), to obtain $S(Q,\omega)$ from those simulation techniques, like FK-LPI and FK-QCW, which provide $\mathrm{Re}F(Q,t)$ as primary output.

Finally, it is useful to summarize how to model the single-molecule lineshape $S_{\mathrm{s}}(Q,\omega)$ in calculations of the quantity $J_{\mathrm{s}}(Q,\omega)$ of Eq. (6). As mentioned in the introduction, the most reliable method at present consists, as we did in other works [10,11], in exploiting quantum RPMD or CMD simulations of the Kubo velocity autocorrelation function, which is defined as

$$u_{\mathrm{K}}(t)=\frac{1}{N}\sum_{i=1}^{N}\frac{1}{\beta}\int_0^\beta d\lambda\,\langle e^{\lambda H}\boldsymbol{v}_i(0)\,e^{-\lambda H}\cdot\boldsymbol{v}_i(t)\rangle, \tag{16}$$

where $\boldsymbol{v}_i(t)$ is the velocity of the center of mass of the $i$th molecule at time $t$. Simulations of the above quantity and calculation of the corresponding spectrum $Z_{\mathrm{K}}(\omega)$ can be used to evaluate the center-of-mass self intermediate scattering function $F_{\mathrm{s}}(Q,t)$ within the Gaussian approximation (GA) [20]. Such an approximation consists in extending the Gaussian $Q$ behavior of this function, which is exact in the hydrodynamic ($Q\to 0$, $t\to\infty$) and free particle ($Q\to\infty$, $t\to 0$) regimes [42], to all times and $Q$ values, according to

$$F_{\mathrm{s}}^{\mathrm{GA}}(Q,t)=e^{-Q^2\gamma_1(t)},\quad\forall\,Q,t, \tag{17}$$

where, according to Rahman *et al.* [21], $\gamma_1(t)$ can be written as

$$\gamma_1(t)=\frac{\hbar}{2M}\int_0^{+\infty}d\omega\,\frac{f(\omega)}{\omega}A(t,\omega), \tag{18}$$

with

$$A(t,\omega)=[1-\cos(\omega t)]\coth\left(\frac{\beta\hbar\omega}{2}\right)-i\sin(\omega t),$$

and

$$f(\omega)=\frac{2M\beta}{3}Z_{\mathrm{K}}(\omega).$$

More precisely, following Rahman and coworkers [21], $F_{\mathrm{s}}(Q,t)$ can be rigorously expressed in the form of an infinite series

$$F_{\mathrm{s}}(Q,t)=\exp\left[\sum_{p=1}^{\infty}(iQ)^{2p}\gamma_p(t)\right],$$

the first term of which is exactly Eq. (17). Note that the symbol $\beta$ used in Ref. [21] has not the usual meaning of inverse temperature but corresponds to $\beta\hbar/2$ in the present notation.

The previous formalism was adopted to perform the calculation of the quantum $S_{\mathrm{s}}^{\mathrm{GA}}(Q,\omega)$, by simple numerical Fourier transformation of Eq. (17), starting from CMD simulations of $u_{\mathrm{K}}(t)$. Note that this procedure ensures that the single-molecule center-of-mass spectrum has the correct quantum asymmetry. Moreover, the GA guarantees that the first four spectral moments are correctly reproduced [21]. This allowed us to evaluate Eq. (6) and, by subtracting it from the measured DDCS as described in Sec. IV, to access the center-of-mass dynamic structure factor of the liquid.

## III. THE NEUTRON SCATTERING EXPERIMENT

The measurements were performed using the time-of-flight thermal neutron spectrometer BRISP at the Institut Laue Langevin (ILL, Grenoble) [43]. This instrument [44–46] was designed to perform neutron Brillouin scattering experiments, i.e., aimed at probing the low-$Q$ region of the dynamic structure factor of (mainly) disordered systems. In the chosen configuration of the spectrometer (incident energy $E_0 = 83.8$ meV, i.e., wavelength $\lambda_0 = 0.988$ Å, sample-detector distance 4 m), it was possible to span the exchanged wavevector range $4 \leqslant Q \leqslant 14$ nm$^{-1}$.

The thermodynamic state we wanted to investigate was one of those that some of us already studied by both neutron diffraction and PIMC simulations [47]. We focused on the $T = 20.7$ K and $n = 25.40$ nm$^{-3}$ state in the liquid phase of $D_2$, with $n$ denoting the molecular number density. In this way a good knowledge of the static structure factor was guaranteed, with a $Q_\text{p}$ value of 21.0 nm$^{-1}$, so that the above quoted $Q$ range was extended beyond $Q_\text{p}/2$. The desired thermodynamic conditions were obtained by using a gas-handling system provided by the ILL and connecting it, by means of a capillary tube, to the empty sample cell maintained in the BRISP cryostat at the chosen temperature (within ≈0.1 K, for the whole duration of the sample measurements). The sample gas was thus condensed directly into the cell, verifying its entire filling with liquid $D_2$ by carefully monitoring the sudden increase of pressure as soon as the liquid-vapor coexistence region is clearly trespassed on the high-density side. As soon as the chosen sample conditions were achieved, the average of subsequent observations of the temperature and pressure conditions of the sample during data acquisition allows us to report a sample stability, in number density, of the order of $n = 25.5 \pm 0.1$ nm$^{-3}$. The sample container was an aluminium slab, with windows orthogonal to the beam each 1 mm thick, and allowing for a sample thickness of 5 mm. The outer frame of the cell was completely shielded by means of a properly tailored cadmium sheet, in order to avoid unwanted scattering from the container. A boron nitride mask at the entrance wall of the cell was also used to adjust the sample area ($45\times25$ mm$^2$) illuminated by the beam.

The adiabatic speed of sound of the liquid in the mentioned state, $c_\text{s} = 984$ m/s [48], is relatively low with respect to other liquids, e.g., molten metals, we studied on the BRISP spectrometer [49,50], therefore a less energetic neutron beam could have been used in favor of a better energy resolution. However, we preferred to access the much wider energy transfer ranges enabled by the use of the (004) reflection of the pyrolitic-graphite monochromator of the instrument, in order to properly probe also the tails of the spectra and have a better control on the accuracy of the necessary correction procedures typical of neutron scattering on liquid samples, which we will summarize in the next section. Of course, the chosen $E_0$ value allowed us to cover a $Q$ region more extended than the one where simple hydrodynamic behavior [42] is expected.

The resolution in the chosen configuration of BRISP was determined by measuring the signal from a vanadium slab (3 mm thick). After correction of the raw V data for background, self-attenuation, and multiple scattering, the resulting spectra were found to have the expected Gaussian shape, with a full width at half maximum of 3.2 meV, almost independent of $Q$. The so-determined resolution function will be indicated as $R(\omega)$ in the next equations.

The intensities scattered from the various samples (empty cell, vanadium, and liquid $D_2$), which were collected as a function of scattering angle and neutron time of flight, have all been preprocessed by using the routines written specifically for BRISP within the LAMP environment of the ILL [51,52]. Such routines implement the conversion of the measured intensity into a function of the exchanged wave vector $Q$ and frequency $\omega$. The codes are public and easily accessible by downloading the runtime version of LAMP. The next section describes the main steps of the subsequent analysis of the so-collected raw neutron data. In what follows, we will always consider the $D_2$ sample in its normal ortho-para concentration since, in the absence of appropriate catalysts, conversion to the equilibrium concentration at 20.7 K could be excluded within the effective duration (about one day) of the measurements devoted to $D_2$.

## IV. ANALYSIS OF THE NEUTRON DATA

The spectra recorded with liquid $D_2$ inside the cell were first corrected by subtracting the background signal and the scattering from the empty cell, the latter duly modified according to the sample transmission in order to take into account the difference in the signal (from the cell alone) between an empty container measurement and a filled cell one. To properly evaluate the attenuation due to the sample, one must take care of the real scattering cross section of the molecule, whose dependence on incident energy was given in Ref. [11], and whose value, calculated at our incident energy, is $\sigma_{\text{s},D_2} \simeq 8$ b, which is clearly different from the one obtained by simply doubling the scattering cross section of the D nucleus [4] ($\sigma_{\text{s,D}} = 7.64$ b). After these preliminary subtractions, and correction for the sample self-attenuation, the signal from the sample can be written as

$$I^{\text{expt}}(Q,\omega) = I^{(1)}(Q,\omega) + I^{(\text{m})}(Q,\omega), \tag{19}$$

i.e., as the sum of the single scattering contribution $I^{(1)}(Q,\omega)$ and the multiple scattering one $I^{(\text{m})}(Q,\omega)$. We evaluated the second (unwanted) component by means of multidimensional Monte Carlo (MC) integration of appropriate functions we described in detail in Ref. [53]. However, the (unknown) scattering law of the molecule has to be taken into account in the best possible way, and to do this we implemented in the MC integration algorithm the calculation of the DDCS according to Eqs. (5), (6), and (7), using the ideal gas law [38] for $S_\text{s}(Q,\omega)$ and the Sköld approximation [54] for $S(Q,\omega)$. In order to evaluate the latter, i.e.,

$$S(Q,\omega) = S(Q) S_\text{s}\left(\frac{Q}{\sqrt{S(Q)}}, \omega\right), \tag{20}$$

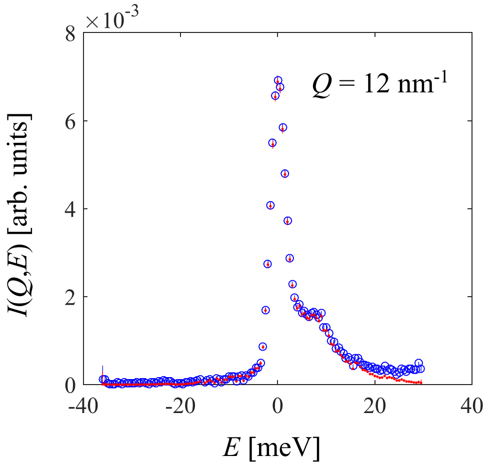

FIG. 1. Effect of the correction for multiple scattering. The raw intensity before the correction (blue circles) is compared with the corrected spectrum (red dots).

we exploited our experimental determination of the static structure factor [47]. Use of the ideal gas law for the center-of-mass self dynamics not only makes the presently rather complex computation of multiple scattering feasible within acceptable times, but also represents a quite reasonable approximation for this kind of correction, given the rather high $Q$ values typically involved in a Monte Carlo integration of multiple scattering events [53]. Figure 1 shows the effect of the correction for multiple scattering at a representative $Q$ value. Differently from the case of very high density liquids, like molten metals, multiple scattering is very small in the present case, but such a correction is useful to bring the spectral tails almost perfectly to zero, without any residual background.

The so-obtained single scattering intensity is the one related to the DDCS of liquid $D_2$ we are interested in, according to

$$\begin{aligned} I^{(1)}(Q,\omega) &= C\frac{d^2\sigma}{d\Omega d\omega}\otimes R(\omega) \\ &= C\left\{\frac{k_1}{k_0}[u(Q)S(Q,\omega)+J_s(Q,\omega)]\right\}\otimes R(\omega), \end{aligned} \tag{21}$$

where we combined Eqs. (5) and (7). In the above equation, $C$ is an instrumental factor. The convolution with the experimental resolution function $R(\omega)$ was also explicitly indicated in order to recall that $I^{(1)}(Q,\omega)$ is affected by resolution broadening.

The determination of $S(Q,\omega)$ from Eq. (21) has been carried out, at each $Q$, through the fitting to the experimental $I^{(1)}(Q,\omega)$ of a convenient model function constructed as follows. A quantum compliant model for $S(Q,\omega)$, described below, is multiplied by the calculated $u(Q)$ and added to $J_s(Q,\omega)$, also calculated as explained at the end of Sec. II. The result is further multiplied by $k_1/k_0$, which in a direct geometry (i.e., at fixed incident energy) spectrometer like BRISP depends on $\omega$ according to $k_1/k_0=\sqrt{1-\omega/\omega_0}$, with $\omega_0=E_0/\hbar$. Finally, the fitted model function includes the convolution with $R(\omega)$. The overall factor $C$ is a free fit parameter.

As far as the $S(Q,\omega)$ modeling is concerned, we applied the Lorentzian multi-mode expansion [34–36] that we detailed and used in several papers [50,55–57], taking into account that, for quantum systems, such an expansion holds for the spectrum of the Kubo-transformed correlation function. Therefore, we used Eq. (12) with $S_K(Q,\omega)$ given by

$$S_K(Q,\omega)=S_K(Q)\sum_{j=1}^{\infty}L_j(\omega)=S_K(Q)\sum_{j=1}^{\infty}\frac{I_j}{\pi}\left[\frac{(-z_j)}{\omega^2+z_j^2}\right], \tag{22}$$

that is, we modeled the Kubo spectrum as a sum of complex Lorentzian lines $L_j(\omega)$. Here, if $I_j$ and $z_j$ are real, then $L_j(\omega)$ is a genuine Lorentzian function centered at $\omega=0$, and characterized by a half width at half maximum equal to $-z_j$, while if $I_j$ and $z_j$ are complex, then the corresponding mode and its complex conjugate add up to give a pair of distorted Lorentzians centered at the nonzero frequencies $\pm\mathrm{Im}\,z_j$, with $\mathrm{Re}z_j<0$ (see Eq. (4) of Ref. [55] for details). This representation in Fourier space of course corresponds to express $F_K(Q,t)$ as a series of complex exponentials in the time domain, i.e., as

$$F_K(Q,t)=F_K(Q,0)\sum_{j=1}^{\infty}I_j\exp(z_j|t|), \tag{23}$$

which better clarifies why, in our notation, $\mathrm{Re}z_j$ must be negative, playing the role of an exponential damping. Clearly, the normalization of $F_K(Q,t)/F_K(Q,0)$ to its initial value leads to the sum rule $\sum_{j=1}^{\infty}I_j=1$, and the existence of its $k$th order ($k=0,1,2,\ldots$) time derivatives at $t=0$ leads, in this exponential representation, to a set of sum rules of the form

$$\sum_{j=1}^{\infty}I_jz_j^k=\left.\frac{d^kF_K(Q,t)}{dt^k}\right|_{t=0}=0 \text{ for odd } k. \tag{24}$$

In a fit procedure, either in the frequency or in the time domain, the series of Eqs. (22) or (23) is of course limited to a small number of terms, with $I_j$ and $z_j$ acting as free parameters. However, some of the amplitudes can be calculated by imposing a certain number of constraints, in order to comply, for instance, with the normalization condition $\sum_j I_j=1$, and to enforce the first few odd sum rules dictated by Eq. (24) up to $k-1$, for a given even $k$. For example, if one has at least three modes, imposing the normalization and the first odd sum rule ensures the convergence of the second spectral moment. When the latter is known, as it is the case for the Kubo dynamic structure factor (see Sec. II), one can also force its second moment not only to be finite, but also to take its theoretical value, via the condition $M_K^{(2)}=-S_K(Q)\sum_j I_jz_j^2=Q^2/(\beta M)$.

As stated above, Eq. (22) represents the multi-Lorentzian expansion of the (symmetric) Kubo spectrum $S_K(Q,\omega)$. In a recent paper [58], we have shown how the parameters $I_j$ and $z_j$ of the various terms of the expansion uniquely determine the modes of the quantum spectrum $S(Q,\omega)$ as well, and how these are modified in order to remove divergences in their frequency integrals. We also showed that the modes of $S(Q,\omega)$ are characterized by the same dampings and frequencies as those of $S_K(Q,\omega)$, indicating that the same relaxation and excitation processes drive the quantum dynamics, while the amplitudes are appropriately modified to produce the correct quantum frequency dependence. Thus, the identification of the various dynamical processes that model the Kubo spectrum and get determined through the fit described above remains valid for the true quantum dynamics as well.

From a practical point of view, the number of real and complex terms, and of sum rules to be imposed is essentially dictated by physical considerations, by the accuracy and extension of the data, and, ultimately, by the quality of the fit achieved by avoiding unjustified overparametrizations or undetermined values of some parameters.

Focusing on the $D_2$ case, and considering the investigated $Q$ range, we do not expect significant deviations from the spectral shape of most liquids, which is usually well described (at very low $Q$) by a generalized hydrodynamic (GH) modeling [59] of $S_K(Q,\omega)$ or (at slightly larger $Q$) by the viscoelastic (VE) lineshape [59]. Both models comply with the general theory of correlation functions [34–36], and represent $S_K(Q,\omega)$, respectively, as: (a) one real mode plus a complex-conjugated pair (3 modes in total) and one imposed odd sum rule, in addition to normalization and (b) two real modes plus one complex-conjugated pair (4 modes in total) and two imposed odd sum rules, again in addition to normalization. In both cases, the clear advantage of using the Lorentzian series representation is that the imposition of physical constraints is straightforward and easy.

Clearly, the real modes are to be identified with the relaxation processes acting in the fluid, while the complex pair accounts for propagating longitudinal acoustic modes. Therefore, in the following, we will also use the more familiar notation [59–61] $z_s = -\mathrm{Re}z$ for the damping of the acoustic (the subscript s here meaning "sound") excitation, and $\omega_s = |\mathrm{Im}z|$ for its frequency, where $z$ indicates the complex frequency of the conjugated pair in the series.

Due to the finite accuracy and resolution of the experimental data, and to the fact that the signal due to collective (propagating and nonpropagating) modes is only a small part of the neutron intensity, we could not properly resolve the fine structure of the central part of the collective spectrum, and only the 3-Lorentzian GH model could be used at all the experimental $Q$ values, even at those where a viscoelastic behavior is physically expected. Therefore, the central width we extracted from the fits cannot be identified with any single relaxation process, but rather with a combination of damping coefficients. Conversely, as shown for other systems [49,50], such an effective model is still able to capture rather well the frequency $\omega_s$ and damping $z_s$ of the sound waves, as alternatively determined, for instance, from viscoelastic fits to smoother and accurate classical simulation results. It is worth stressing that a very important property of this effective modeling of the collective part of the experimental lineshape, and of the consequent fit result, is undoubtedly its full compliance with the second moment sum rule, that we imposed on $M_K^{(2)}$ as explained before. This ensures, via Eq. (13), that the first moment sum rule given in Eq. (9) for the genuine quantum spectrum is finally obeyed by the fitted $S(Q,\omega)$. Such a requirement assumes special importance in the case of low mass and low temperature liquids, since the corresponding spectra are strongly asymmetric. Keeping a high control on the correct asymmetry of the fit results is therefore decisive.

By imposing the mentioned constraints, the free parameters in the model for $S_K(Q,\omega)$ reduce to three, since the amplitudes are determined through the sum rules. As far as the whole fit function of Eq. (21) is concerned, two additional free parameters are to be considered, one of which is the normalization factor. The other, not indicated in the equation, allows for the possible presence of impurities, which we assumed to be $H_2$ because around $E = \hbar\omega = 15$ meV we observed an extra intensity in the measured spectra, which was not well accounted for by the very small signal due to the $J_0 = 1 \rightarrow J_1 = 2$ rotational transition of $D_2$. It is well known, in fact, that the above is also the energy at which the $J_0 = 0 \rightarrow J_1 = 1$ transition of $H_2$ is located. Therefore, we calculated Eq. (6) also for the case of $H_2$ at 20.7 K and considered it in our fits, leaving the percentage of $H_2$ as a free parameter (of course, the percentage of $D_2$ was reduced accordingly). Despite the isotopic purity of the $D_2$ gas was declared to be 99.8% (the chemical purity is usually much higher), the fits at all $Q$ values revealed the presence of $\sim$0.5% of $H_2$.

Figure 2 shows the fit to $I^{(1)}(Q,E)$ at three $Q$ values. We display the results as a function of the exchanged energy $E$ in units of meV, which is more familiar to experimentalists. The various components are also shown separately in order to appreciate the role played by the self contribution, which is dominant over the collective one owing to the very small values that the static structure factor [47] assumes at the low $Q$ values of the present experiment. The experimental (i.e., resolution broadened) $S(Q,\omega)$, obtained from Eq. (21) as

$$S(Q,\omega)\otimes R(\omega)=\frac{1}{u(Q)}\left[\frac{k_0}{k_1}\frac{I^{(1)}(Q,\omega)}{C} - J_s(Q,\omega)\otimes R(\omega)\right], \tag{25}$$

is reported in Fig. 3, along with the collective component of the previous fit to $I^{(1)}(Q,E)$. Note that, since the ratio $k_1/k_0$ depends on frequency, Eq. (25) follows from Eq. (21) only if the quantities $[\frac{k_1}{k_0}S(Q,\omega)]\otimes R(\omega)$ and $\frac{k_1}{k_0}[S(Q,\omega)\otimes R(\omega)]$ coincide, which we verified to hold true in our case to a very good approximation. The resolution broadened simulation results obtained by the mentioned methods, and described in the next section, are also shown in Fig. 3. With the exception of the FK-LPI results, comparison of the broadened quantities indicates that the RPMD and FK-QCW simulations are compatible with the neutron data, although as $Q$ grows they appreciably differ from each other and from the fit result, especially as far as the inelastic peak is concerned. At this level, one could state that the agreement between the neutron data points and RPMD/FK-QCW is of the same quality of that shown for $D_2$ in Refs. [31] and [32]. More detailed comparisons between the absolute scale (and resolution free) experimental and computational data will be shown in Sec. VI, after a brief description of the approximations involved in each of the used simulation algorithms to which the following section is devoted.

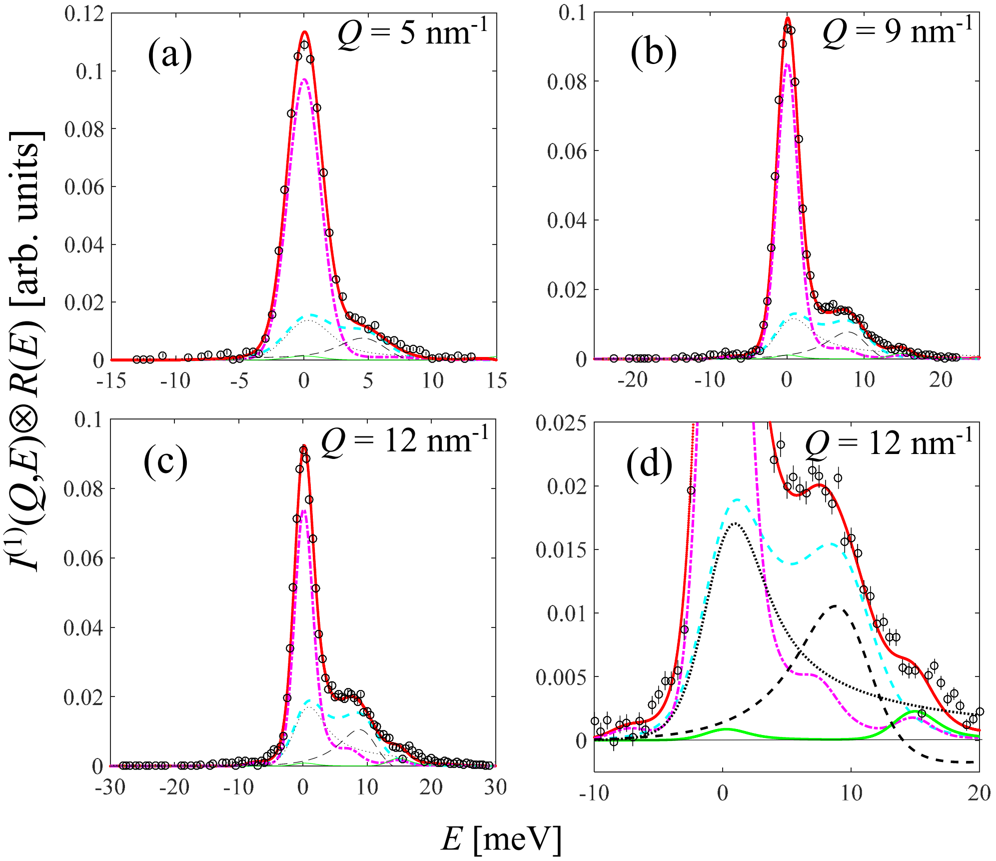

FIG. 2. [(a)–(c)] Fully corrected single scattering intensity from the $D_2$ liquid sample (black circles with error bars) at the $Q$ values specified in each panel. The fit of Eq. (21) to the neutron data (full-red curve) was based on a GH modeling [59] of $S_K(Q,\omega)$ with the explicit imposition of the exact value of $M_K^{(2)}$, which ensures, via Eq. (13), the conformance to the quantum sum rule dictated by Eq. (9). The quantum fit result for $S(Q,\omega)$ is displayed as a cyan-dashed curve. Its elastic (black-dotted curve) and inelastic (black-dashed curve) contributions, adding up to the cyan curve, are also shown. The dominant component, as far as the central part of the neutron spectrum is concerned, is the contribution of the single-molecule term (magenta dot-dashed curve) we calculated as explained in the text, and normalized according to the fitted $C$ of Eq. (21). Finally, the green-thin curve accounts for a ~0.5 % presence of $H_2$ impurities allowing to better reproduce the experimental data around the almost coinciding energies (15 meV) pertaining to both the $1 \to 2$ rotational transition of $D_2$ and the $0 \to 1$ one of $H_2$. Details can be better appreciated in panel (d), which displays a zoom of panel (c).

## V. COMPUTER SIMULATIONS

### A. RPMD

Ring polymer molecular dynamics certainly is the most straightforward approach to simulating the dynamics of moderate quantum systems and consists in replacing, in the case of a system of spherical particles obeying Boltzmann statistics, each quantum particle by a classical ring polymer of $P$ copies of itself, where successive monomers on the same polymer are connected by harmonic springs, with spring constants determined by $\beta$, $\hbar$, and the mass $m$ of the particles [16–18]. Thus the Hamiltonian of the equivalent classical system is

$$H = \frac{1}{P}\sum_{k=1}^{P}\left\{\sum_{j=1}^{N}\left[\frac{1}{2m_j}\left(\boldsymbol{p}_j^{(k)}\right)^2 + \frac{m_j P^2}{2\beta^2\hbar^2}\left(\boldsymbol{r}_j^{(k+1)} - \boldsymbol{r}_j^{(k)}\right)^2\right] + V\left(\boldsymbol{r}_1^{(k)},\ldots,\boldsymbol{r}_N^{(k)}\right)\right\}, \tag{26}$$

and, in principle, the limit $P \to \infty$ should be taken. In Eq. (26), $j$ labels particles (polymers), $k$ monomers, $\boldsymbol{r}_j^{(P+1)} \equiv \boldsymbol{r}_j^{(1)}$, and only monomers with the same index $k$ are allowed to interact through the intermolecular potential $V$.

Since, in RPMD, expectations of operators depending on positions are defined as averages over the monomers of each polymer, time correlation functions are calculated along trajectories as

$$\langle \hat{A}(0)\hat{B}(t)\rangle_K \approx \left\langle\left[\frac{1}{P}\sum_{k=1}^{P} A\left(\boldsymbol{r}_1^{(k)}(0),\ldots,\boldsymbol{r}_N^{(k)}(0)\right)\right]\left[\frac{1}{P}\sum_{k'=1}^{P} B\left(\boldsymbol{r}_1^{(k')}(t),\ldots,\boldsymbol{r}_N^{(k')}(t)\right)\right]\right\rangle, \tag{27}$$

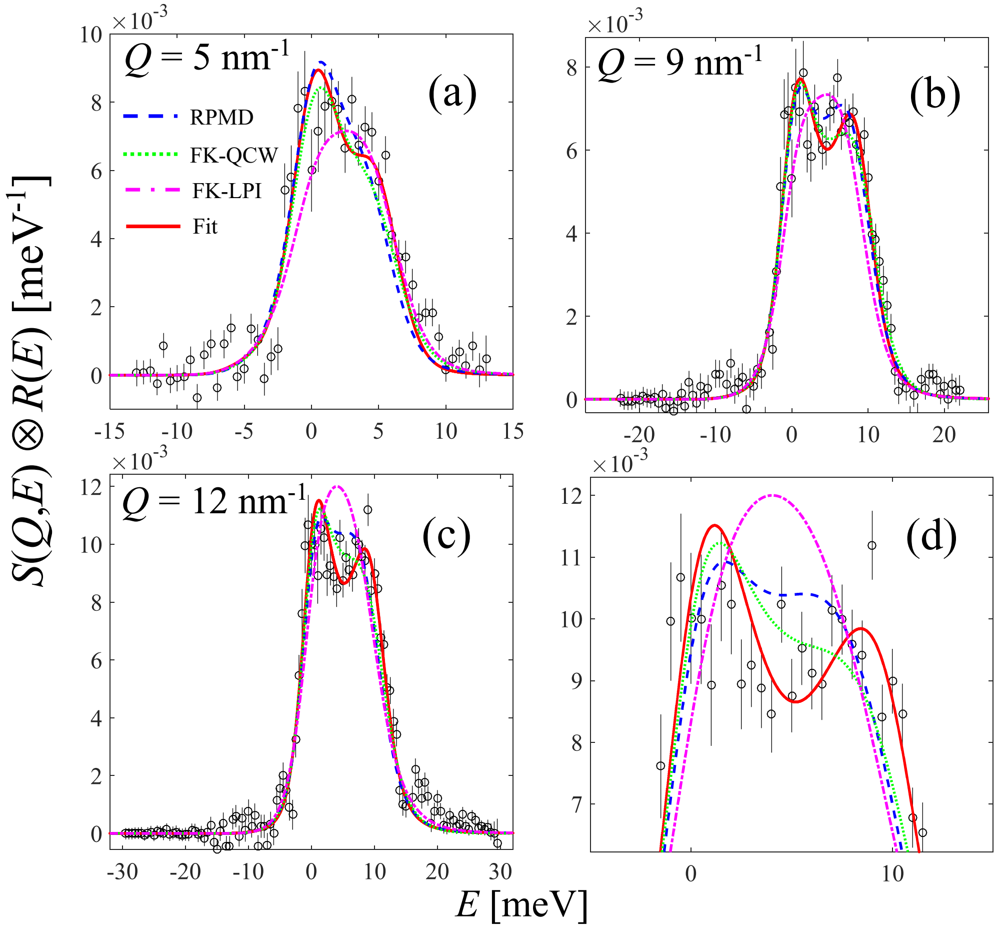

FIG. 3. [(a)–(c)] Experimental dynamic structure factor (black circles with error bars) obtained from Eq. (25). This quantity is in absolute units, although still affected by the experimental energy resolution. The red full line is the component due to collective modes resulting from the fit to $I^{(1)}(Q,E)$, i.e., apart from the factor $Ck_1u(Q)/k_0$, corresponds to the cyan dashed curve of Fig. 2. Comparison is also made with the three different simulations of the quantum $S(Q,E)$ broadened by the instrumental resolution function: RPMD (blue-dashed line), FK-QCW (green-dotted line), and FK-LPI (dot-dashed magenta line). To better distinguish the different results for the central part of the spectrum we show in panel (d) a zoom of panel (c).

where $A$ and $B$ are the classical functions corresponding to operators $\hat{A}$ and $\hat{B}$, and we have indicated that it is the Kubo transform of the correlation function to which the direct output of RPMD provides an approximation, so that, in order to obtain the genuine quantum mechanical correlations and spectra, one must invert the transform using Eq. (12).

One problem with naive RPMD is that the frequencies of the polymers' internal modes, which are a purely mathematical device, may leak into the physical spectra. As in our previous paper on the velocity correlation function of $H_2$ (see Ref. [1]), we have therefore assigned optimally damped Langevin thermostats [62] to all noncentroid modes when integrating the equations of motion, while the translational kinetic energy of the polymers' centroids was controlled by stochastic velocity scaling [63] with a relaxation time $\tau = 20\,\text{ps}$. Using a timestep $\Delta t = 0.001\,\text{ps}$ and a Trotter number $P = 32$, we have performed 20 independent 10 ns simulations with a system of $N = 256$ polymers interacting through the Silvera–Goldman potential [19], as well as 10 analogous runs with a larger sample of $N = 864$ particles, averaging the results over the subruns. The Kubo intermediate scattering function was calculated for all wave vectors $\boldsymbol{Q}$ compatible with the cubic simulation volume such that $Q < 20\,\text{nm}^{-1}$.

On the other hand, one of the fundamental limitations of RPMD is that it may not be expected to work well for correlation functions of operators, which are nonlinear functions of the coordinate or momenta such as Eqs. (2) and (3), and this has been demonstrated early on [64] for the case of the self-intermediate scattering function of $H_2$. However, as far as the static structure is concerned, we find that, in our restricted range of wave vectors, RPMD provides the correct result. In fact, Fig. 4 shows that, although the Kubo structure factor $S_K(Q) \equiv F_K(Q,0)$ falls well below the $S(Q)$ from a reference PIMC simulation with the same Trotter number and number of particles, once it is "corrected" by converting it to the genuine $F(Q,0)$ [cf. the discussion following Eq. (11)], RPMD is in perfect accord with PIMC. Of course, agreement with the correct quantum static structure is only a necessary condition, which does not guarantee that the time dependence of $F(Q,t)$ will also be reproduced correctly by RPMD.

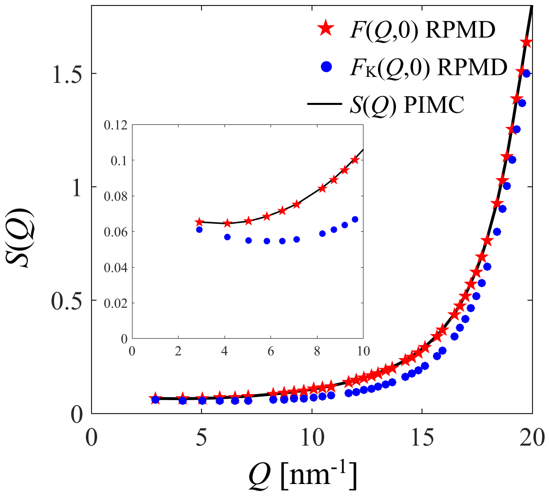

FIG. 4. Static structure factor of D$_2$ at $T = 20.7\,\mathrm{K}$, $n = 25.40\,\mathrm{nm}^{-3}$, obtained from simulations with $N = 256$ particles and Trotter number $P = 32$. Red-full stars: $S(Q) = F(Q, 0)$ from RPMD; blue-full circles: $S_\mathrm{K}(Q) = F_\mathrm{K}(Q, 0)$ from RPMD; black-solid line: $S(Q)$ from PIMC.

### B. FK-LPI

In contrast to RPMD, the Feynman–Kleinert linearized path-integral method [30,65–68] is not limited to operators, which are linear in the coordinates or momenta, and its output is the genuine quantum mechanical correlation function itself, rather than the Kubo transform.

The approximation involved is

$$\langle\hat{A}(0)\hat{B}(t)\rangle \approx \frac{1}{(2\pi\hbar)^{3N}Z}\int d\boldsymbol{q}\,d\boldsymbol{p}$$
$$\times\,[\mathrm{e}^{-\beta\hat{H}}\hat{A}]_\mathrm{W}(\boldsymbol{q},\boldsymbol{p})\,[\hat{B}]_\mathrm{W}(\boldsymbol{q}_t,\boldsymbol{p}_t), \qquad (28)$$

where $\boldsymbol{q}$ and $\boldsymbol{p}$ are the collective Cartesian coordinates and momenta arranged in the order $\boldsymbol{q} = (x_1, y_1, z_1, x_2, y_2, z_2, \ldots)$, $Z$ is the partition function, $[\ldots]_\mathrm{W}$ denotes the Wigner transform of an operator, and $(\boldsymbol{q}_t, \boldsymbol{p}_t)$ is a phase space point on the classical trajectory starting from $(\boldsymbol{q}, \boldsymbol{p})$.

The basis of the algorithm is a Monte Carlo random walk in the space of the particles' "center" coordinates $\boldsymbol{q}_c$, governed by the Boltzmann factor $\exp[-\beta W_1(\boldsymbol{q}_c)]$ of the effective potential

$$W_1(\boldsymbol{q}_c) = \frac{1}{\beta}\sum_{n=1}^{3N}\ln\left\{\frac{\sinh[\beta\hbar\omega_n(\boldsymbol{q}_c)/2]}{\beta\hbar\omega_n(\boldsymbol{q}_c)/2}\right\}$$
$$+\,V_A(\boldsymbol{q}_c) - \frac{1}{2}\sum_{n=1}^{3N}\lambda_n(\boldsymbol{q}_c)\,\omega_n^2(\boldsymbol{q}_c). \qquad (29)$$

Here, $V_A$ is a Gaussian-smeared version of the potential energy $V$ of the system,

$$V_A(\boldsymbol{q}_c) = \int d\boldsymbol{q}\,\frac{1}{\sqrt{\det\left(2\pi\boldsymbol{A}(\boldsymbol{q}_c)\right)}}$$
$$\times\,\exp\left\{-\frac{1}{2}(\boldsymbol{q}-\boldsymbol{q}_c)^T\boldsymbol{A}^{-1}(\boldsymbol{q}_c)(\boldsymbol{q}-\boldsymbol{q}_c)\right\}V(\boldsymbol{q}), \quad (30)$$

$$\lambda_n(\boldsymbol{q}_c) = \frac{1}{\beta\,\omega_n^2(\boldsymbol{q}_c)}\left[\frac{\beta\hbar\omega_n(\boldsymbol{q}_c)}{2}\coth\left(\frac{\beta\hbar\omega_n(\boldsymbol{q}_c)}{2}\right) - 1\right], \qquad (31)$$

and $\omega_n^2(\boldsymbol{q}_c)$ are the eigenvalues of the Feynman–Kleinert effective frequency matrix

$$\Omega^2(\boldsymbol{q}_c) = \int d\boldsymbol{q}\,\frac{1}{\sqrt{\det\left(2\pi\boldsymbol{A}(\boldsymbol{q}_c)\right)}}$$
$$\times\,\exp\left\{-\frac{1}{2}(\boldsymbol{q}-\boldsymbol{q}_c)^T\boldsymbol{A}^{-1}(\boldsymbol{q}_c)(\boldsymbol{q}-\boldsymbol{q}_c)\right\}$$
$$\times\,\boldsymbol{M}^{-1/2}\boldsymbol{H}(\boldsymbol{q})\boldsymbol{M}^{-1/2}, \qquad (32)$$

where $\boldsymbol{H}_V$ is the Hessian (matrix of second derivatives) of $V$, and $\boldsymbol{M}$ is the diagonal matrix of particle masses. The smearing-width matrix $\boldsymbol{A}$ and the frequencies $\omega_n^2$ are determined iteratively by solving the last equation in conjunction with

$$\boldsymbol{A}(\boldsymbol{q}_c) = \boldsymbol{M}^{1/2}\,\boldsymbol{U}(\boldsymbol{q}_c)\,\boldsymbol{\Lambda}\,\boldsymbol{U}^T(\boldsymbol{q}_c)\,\boldsymbol{M}^{1/2}, \qquad (33)$$

where $\boldsymbol{\Lambda} = \mathrm{diag}(\lambda_1, \lambda_2, \ldots)$, and $\boldsymbol{U}(\boldsymbol{q}_c)$ is the transformation, which diagonalizes $\boldsymbol{\Omega}^2(\boldsymbol{q}_c)$. $\boldsymbol{U}(\boldsymbol{q}_c)$ also defines the mass-weighted instantaneous normal modes and momenta of the system

$$\boldsymbol{\eta} = \boldsymbol{U}^T(\boldsymbol{q}_c)\boldsymbol{M}^{1/2}\boldsymbol{q}, \qquad (34)$$

$$\boldsymbol{\eta}_c = \boldsymbol{U}^T(\boldsymbol{q}_c)\boldsymbol{M}^{1/2}\boldsymbol{q}_c, \qquad (35)$$

$$\boldsymbol{\nu} = \boldsymbol{U}^T(\boldsymbol{q}_c)\boldsymbol{M}^{-1/2}\boldsymbol{p}. \qquad (36)$$

Periodically during the random walk, $P$ independent sets of normal mode positions and momenta $(\boldsymbol{\eta}, \boldsymbol{\nu})$ are drawn from the probability density

$$f(\boldsymbol{\eta},\boldsymbol{\nu}) = \prod_{n=1}^{3N}\frac{1}{\pi\hbar}\sqrt{\frac{\tanh\left(\beta\hbar\omega_n(\boldsymbol{q}_c)/2\right)}{\alpha_n(\boldsymbol{q}_c)}}$$
$$\times\,\exp\left\{-\frac{\omega_n(\boldsymbol{q}_c)}{\hbar\alpha_n(\boldsymbol{q}_c)}(\eta_n - \eta_{c,n})^2\right.$$
$$\left.-\,\frac{\tanh(\beta\hbar\omega_n(\boldsymbol{q}_c)/2)}{\hbar\omega_n(\boldsymbol{q}_c)}\nu_n^2\right\}, \qquad (37)$$

with

$$\alpha_n(\boldsymbol{q}_c) = \coth\left(\frac{\beta\hbar\omega_n(\boldsymbol{q}_c)}{2}\right) - \frac{2}{\beta\hbar\omega_n(\boldsymbol{q}_c)}, \qquad (38)$$

which when converted to Cartesian coordinates with the help of Eqs. (34) and (36), define a "swarm" of phase points $(\boldsymbol{q}, \boldsymbol{p})$ in the spatial neighborhood of the current $\boldsymbol{q}_c$. Using these as initial conditions, the system's equations of motion are integrated classically (involving the original potential $V$) up to the desired maximum time lag of the correlation function.

While the Wigner transform of the terms corresponding to time $t$ in the intermediate scattering function,

$$F(\boldsymbol{Q},t) = \frac{1}{N}\left\langle\sum_{j=1}^{N}\mathrm{e}^{-i\boldsymbol{Q}\cdot\hat{\boldsymbol{r}}_j(0)}\sum_{\ell=1}^{N}\mathrm{e}^{i\boldsymbol{Q}\cdot\hat{\boldsymbol{r}}_\ell(t)}\right\rangle, \qquad (39)$$

is simply $\mathrm{e}^{i\boldsymbol{Q}\cdot\boldsymbol{r}_\ell(t)}$, i.e., with the position operator of particle $\ell$ replaced by the classical variable $\boldsymbol{r}_\ell$, the analogous terms at $t = 0$ may be written in the form $w_j(\boldsymbol{Q}, \boldsymbol{q}_c)_j \mathrm{e}^{-i\boldsymbol{Q}\cdot\boldsymbol{r}_j(0)}$, where the "weight factors" [69],

$$w_j(\boldsymbol{Q}, \boldsymbol{q}_c) = \prod_{n=1}^{3N} \exp\left\{-\frac{\tanh\left(\beta\hbar\omega_n(\boldsymbol{q}_c)/2\right)}{\hbar\omega_n(\boldsymbol{q}_c)} \times \left[\nu_n - \frac{\hbar}{2}\, m_j^{-1/2}\left(Q_x\, U(\boldsymbol{q}_c)_{3(j-1)+1} + Q_y\, U(\boldsymbol{q}_c)_{3(j-1)+2} + Q_z\, U(\boldsymbol{q}_c)_{3(j-1)+3}\right)\right]^2\right\}, \tag{40}$$

correct for the fact that $f(\boldsymbol{\eta}, \boldsymbol{\nu})$ samples from $[\mathrm{e}^{-\beta\hat{H}}]_\mathrm{W}$, rather than from $[\mathrm{e}^{-\beta\hat{H}}\mathrm{e}^{-i\boldsymbol{Q}\cdot\hat{\boldsymbol{r}}_j(0)}]_\mathrm{W}$, as required by Eq. (28).

We have performed FK-LPI simulations of $D_2$ with systems of $N = 108$ and $N = 256$ particles interacting through the Silvera–Goldman potential [19]. As in Ref. [66], the SG potential was represented by a sum of four Gaussians, in order to facilitate the convolution of the Hessian in Eq. (32), and the resulting effective frequency matrix $\Omega^2(\boldsymbol{q}_c)$ was diagonalized with the help of the LAPACK [70] procedure `dsyevr`. Since this is the most time-consuming step, the random walk in $\boldsymbol{q}_c$-space was based on all-particle (rather than single-particle) moves in the usual Metropolis Monte Carlo procedure [71]. In the case of the $N = 108$ system, sets of $P = 32$ ($P = 128$) initial conditions were, in two separate random walks consisting of 20 independent subchains each, sampled every 50 (10) moves out of a total of $10^6$ ($2\times10^6$) configurations, and the classical swarm trajectories were followed for 10 ps using the velocity Verlet algorithm [71] with a timestep of $\Delta t = 0.002$ ps. For the larger $N = 256$ system, sets of $P = 128$ initial conditions were sampled every 10 moves, but the random walk was only extended for a total $2\times10^5$ steps. As with RPMD, the intermediate scattering function was calculated for all wave vectors compatible with the cubic simulation volume.

In a disordered system, some of the mode frequencies $\omega_n(\boldsymbol{q}_c)$ will turn out to be imaginary. However, the prefactors of the modes' positions and momenta in the exponent of Eq. (37)—the latter factor also appears in Eq. (40)—may be shown to remain well defined and positive as long as $|\omega_n(\boldsymbol{q}_c)| < 2\pi/(\beta\hbar)$ and $|\omega_n(\boldsymbol{q}_c)| < \pi/(\beta\hbar)$, respectively (in the latter case one may put $\nu_n = 0$). We have not observed that even the more stringent restriction is ever violated for $D_2$ in the present thermodynamic state.

### C. FK-QCW

The Feynman–Kleinert quasiclassical Wigner method [32,33] has been proposed to correct one of the perceived shortcomings of FK-LPI, namely that thermodynamic properties are not conserved along the swarm trajectories. FK-QCW [72] is closely related to FK-LPI and makes use of the identical ansatz Eq. (28) for the correlation function, as well as of the concept of center and swarm—here, more aptly called "satellite"—trajectories. However, instead of being generated by a random walk, the particles' centers are now propagated quasiclassically according to the equations of motion

$$\dot{\boldsymbol{p}}_c = -\nabla_c\,[V_A(\boldsymbol{q}_c)], \tag{41}$$

$$\dot{\boldsymbol{q}}_c = \boldsymbol{M}^{-1}\boldsymbol{p}_c, \tag{42}$$

where $\boldsymbol{p}_c$ are the momenta associated with $\boldsymbol{q}_c$, $V_A$ is again the smeared potential of Eq. (30), and the gradient with respect to the center coordinates in Eq. (41) is taken keeping the smearing-width matrix constant [73].

As in FK-LPI, initial conditions for the satellite trajectories are sampled, in terms of normal coordinates and momenta, from Eq. (37), but instead of evolving independently under the influence of the original potential $V$, the satellites are now coupled to ("orbiting around") the center trajectory through

$$\boldsymbol{q} = \boldsymbol{q}_c + \boldsymbol{M}^{-1/2}\boldsymbol{U}(\boldsymbol{q}_c)(\boldsymbol{\eta} - \boldsymbol{\eta}_c), \tag{43}$$

$$\boldsymbol{p} = \boldsymbol{M}^{1/2}\boldsymbol{U}(\boldsymbol{q}_c)\,\boldsymbol{\nu}, \tag{44}$$

and follow the equations of motion

$$\dot{\tilde{q}}_n = f_n(\boldsymbol{q}_c)\,\tilde{p}_n, \tag{45}$$

$$\dot{\tilde{p}}_n = -f_n(\boldsymbol{q}_c)\,\tilde{q}_n. \tag{46}$$

Here, $(\tilde{q}_n, \tilde{p}_n)$ are dimensionless normal mode coordinates related to $(\eta_n, \nu_n)$ by

$$\tilde{q}_n = \sqrt{\frac{\omega_n(\boldsymbol{q}_c)}{\hbar\alpha_n(\boldsymbol{q}_c)}}\,(\eta_n - \eta_{c,n}), \tag{47}$$

$$\tilde{p}_n = \sqrt{\frac{\tanh\left(\beta\hbar\omega_n(\boldsymbol{q}_c)/2\right)}{\hbar\omega_n(\boldsymbol{q}_c)}}\,\nu_n \tag{48}$$

[cf. the prefactors in the exponentials of Eq. (37)], and [74]

$$f_n(\boldsymbol{q}_c) = \begin{cases} \omega_n(\boldsymbol{q}_c) & \text{for} \quad \omega_n^2(\boldsymbol{q}_c) \geqslant 0, \\ 0 & \text{otherwise.} \end{cases} \tag{49}$$

An FK-QCW simulation consists of a sequence of center trajectories, where, at the beginning of each trajectory, initial normal mode coordinates and momenta are sampled from Eq. (37) for $P$ satellites, and the satellites' equations of motion are integrated up to the maximum time lag desired for the correlation function. As with FK-LPI, each satellite's $t = 0$ value of the observable $A$ must be multiplied by a weight factor such as Eq. (40) before correlating it with $B$ at a later time. In contrast to FK-LPI, however, FK-QCW is only expected to provide an approximation to the real (not the imaginary) part of the quantum mechanical correlation function.

Our implementation of FK-QCW closely followed the recipe given in the Appendix of Ref. [32], except Eqs. (A2) and (A3), which we replaced by the exact harmonic oscillator solution, rather than using the explicit Euler scheme, which is unstable. Similarly to the case of FK-LPI, we performed

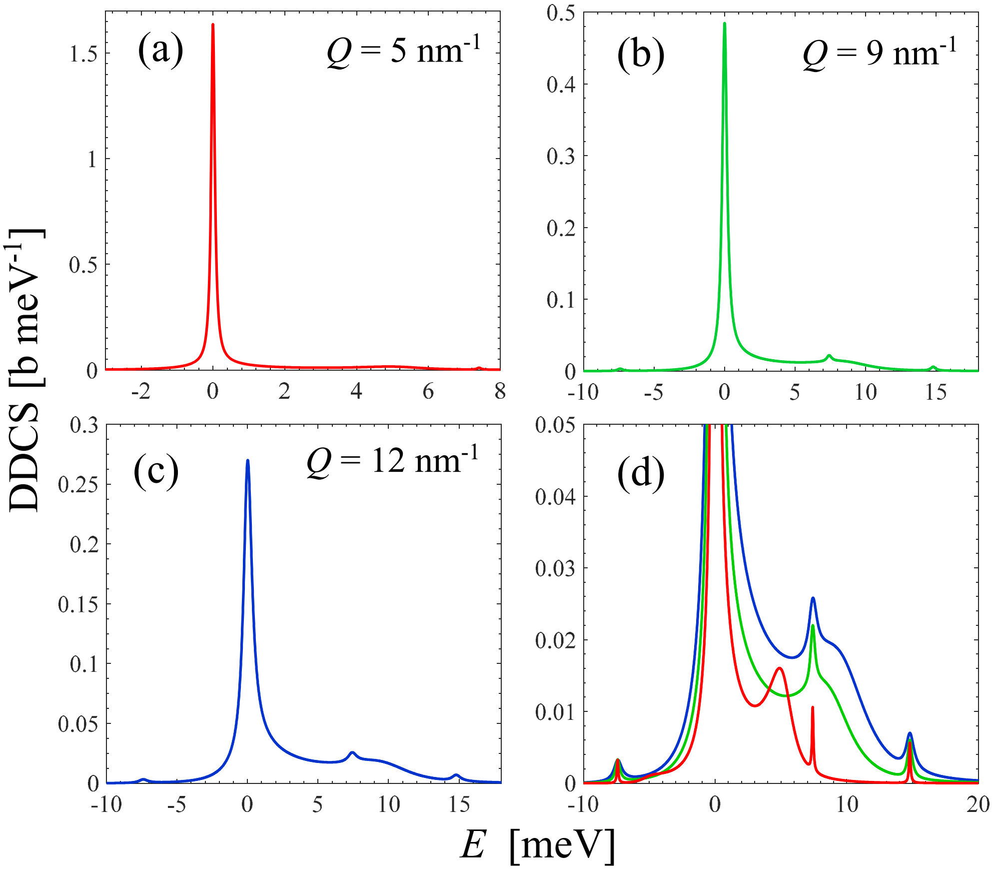

FIG. 5. [(a)–(c)] Resolution free double differential cross section of liquid $D_2$ at 20.7 K at three typical $Q$ values, as obtained from the fits to $I^{(1)}(Q,\omega)$ explained in the text. The displayed quantity is in absolute units. Note the very different amplitudes and widths of the spectra with increasing $Q$. (d) Zoom of the three spectra shown in panels [(a)–(c)] in order to better appreciate how the Brillouin peak (clearly visible at 5 $\mathrm{nm}^{-1}$, red curve) evolves as $Q$ grows, and tends to merge with the $0 \rightarrow 1$ rotational line. Also visible are the low-intensity $1 \rightarrow 0$ and $1 \rightarrow 2$ lines at –7.4 meV and 14.8 meV, respectively.

simulations with systems of $N = 108$ as well as $N = 256$ (center) particles, with $P = 32$ satellites orbiting the central trajectory. The time step was again set to $\Delta t = 0.002$ ps, and individual trajectories were extended to 10 ps. For the smaller system, the simulation was broken up into 20 independent runs of 500 consecutive trajectories, while for the larger system it consisted of 100 runs of 100 trajectories, bringing to total up to $10^4$ trajectories in either case.

For the comparison with experiment and for the analysis described in the next section the results obtained for the larger systems have been used.

## VI. COLLECTIVE DYNAMICS OF LIQUID $D_2$

As mentioned, our objective was to show both the neutron DDCS and $S(Q,\omega)$ free from resolution effects and in absolute units [75]. Therefore, we report in Fig. 5 the DDCS as obtained from the sum of the calculated $J_s(Q,\omega)$ and $u(Q)S(Q,\omega)$, with $S(Q,\omega)$ directly obtained from the fit output parameters. $S(Q,\omega)$ is finally shown in Fig. 6, together with the dynamic structure factors obtained by the RPMD, FK-LPI, and FK-QCW simulation methods described in the preceding section. In order to perform a correct comparison, completely free from resolution effects, the calculated spectra were obtained by Fourier transformation of the quantum $F(Q,t)$ without applying any windowing, which differently would give rise to a broadening of the simulated spectrum.

Turning to the comparisons of Fig. 6, these definitely show a less than perfect agreement of the experimental results with all the simulated $S(Q,\omega)$'s, which is particularly pronounced in the FK-LPI case. On the whole, the experimental spectra display quite a marked contribution of the acoustic excitations, visibly less damped and located, at a first glance, at slightly larger energies than those predicted by the RPMD and FK-QCW simulations. Visual inspection of the position and width of inelastic spectral contributions in so asymmetrical spectra can, however, be deceptive. Therefore, a detailed comparison of the characteristic features of collective excitations and relaxations in liquid $D_2$, as found from our experiment and as predicted by RPMD and FK-QCW simulations, will be given in the remainder of this section. The complementary behavior in the time domain is shown in Fig. 7. The curves represent the Kubo intermediate scattering function at $Q = 12\ \mathrm{nm}^{-1}$, as obtained from the (resolution-free) fit to the neutron data and from the various simulation methods, using the same line and color codes of Fig. 6. As deducible also from the spectra of Fig. 6, the $F_K(Q,t)$ derived from simulations are visibly more damped and display a less marked oscillatory behavior than the one obtained from experiment.

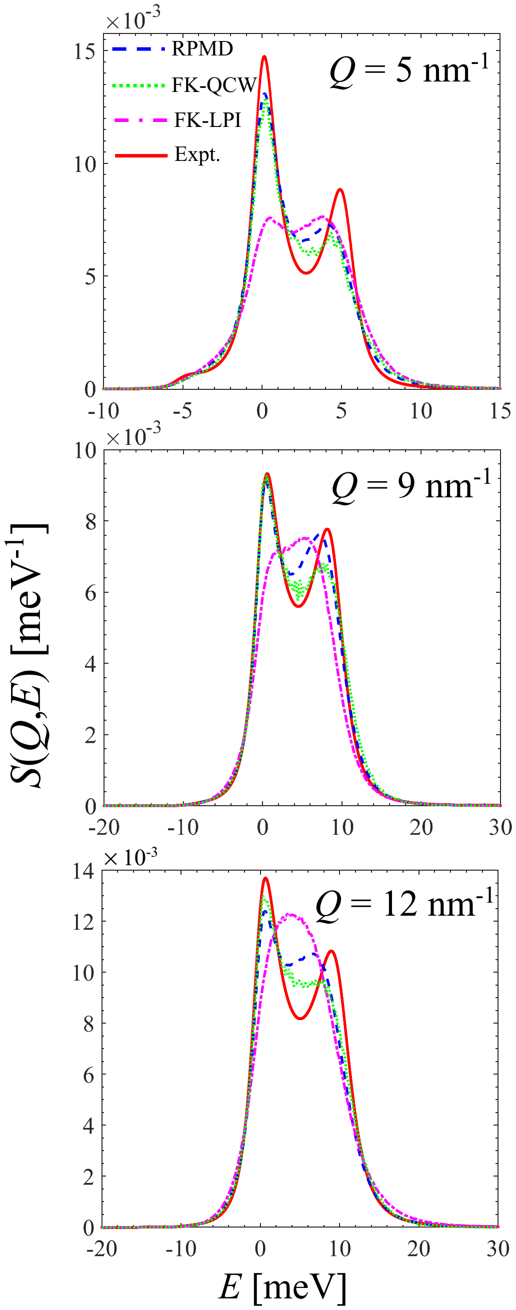

FIG. 6. Resolution free dynamic structure factor obtained from the fit to the neutron data (red-solid line) compared with three different evaluations of the quantum $S(Q, E)$: RPMD (blue-dashed line), FK-QCW (green -dotted line), and FK-LPI (dot-dashed magenta line). Note that FK-QCW performs better than RPMD at $Q = 9\ \text{nm}^{-1}$.

These results indicate that the way sound modes are reproduced by different quantum simulation methods is a key point in the discrepancies, not only with experiment but also among different simulation algorithms. Conversely, a better overall agreement, except for the FK-LPI case, is observed from Fig. 6 as far as the nonpropagating modes are concerned, both at the experimental and simulation level. In any case, as mentioned in the previous section, each one of the various calculation methods that are compared here with the experimental results is based on some approximation whose effects are not easy to evaluate.

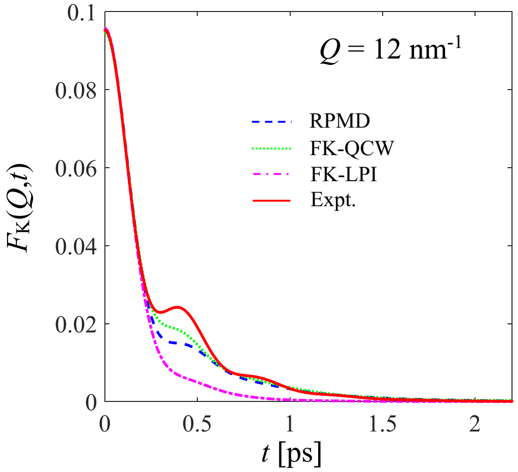

FIG. 7. Kubo intermediate scattering function derived from the fit to the experimental data at $Q = 12\ \text{nm}^{-1}$ (red-solid line) compared with the corresponding RPMD (blue-dashed line), FK-QCW (green-dotted line), and FK-LPI (dot-dashed magenta line) estimates.

The RPMD and FK-QCW results for $S(Q, \omega)$, although not quantitatively matching the experiment seem definitely more realistic than the unimodal ones obtained by means of FK-LPI simulations. We therefore decided to analyze in detail the dynamical properties deducible from these two calculation methods, in comparison with those derived from the neutron data. From a numerical point of view, simulations can provide much more accurate and smoother results than experiment, so, as it often happens, they allow the use of fit models (with more parameters than the GH one), which better represent the behavior of a liquid at the length scales probed in this investigation. In the $Q$ range of the present study, a viscoelastic behavior is indeed expected.

As already stated in Sec. IV, the VE model is implemented by assuming two real modes (hereinafter labeled as R1 and R2) and one complex pair in the series, and by ensuring the finiteness of the fourth spectral moment, a condition, which is enforced by imposing, beyond normalization, the first two odd sum rules. Correspondingly, the VE spectrum consists of four lines, i.e., it has an additional central Lorentzian with respect to the GH model [59].

The VE model has been fitted to the RPMD Kubo intermediate scattering function up to a maximum time value $t_\mathrm{R} = 2.2$ ps, which is the so called recurrence time due to the use of periodic boundary conditions in the simulations [2,71]. The recurrence time is roughly the maximum time lag beyond which the calculations are no more reliable and typically present spurious oscillations [76]. Such a cutoff turned out, instead, to be not restrictive enough to exclude some small unphysical signal from the reliable fitting window of the FK-QCW case, where we limited to 1.5 ps the upper bound of the fit range.

Figures 8 and 9 show that a VE modeling excellently accounts for the RPMD shape of $F_\mathrm{K}(Q, t)$, and of the corresponding spectrum. Moreover, the semilogarithmic plots of Fig. 10 indicate that a simpler GH modeling of the RPMD

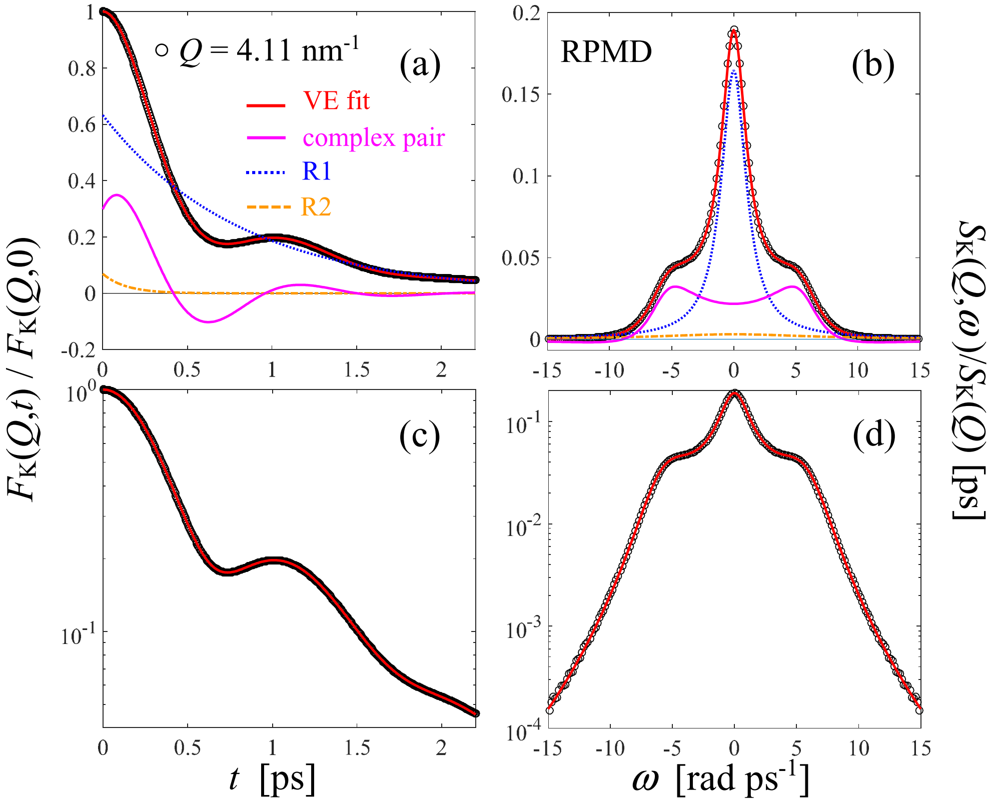

FIG. 8. (a) RPMD estimate of the Kubo intermediate scattering function $F_K(Q, t)$ of liquid $D_2$ at $Q = 4.11$ nm$^{-1}$ (black circles) and VE fit result (red-solid curve). Note the change of the spectral variable with respect to previous figures. The multi-exponential fit components are also shown separately, and specified in the legend. (b) Corresponding spectrum $S_K(Q, \omega)/S_K(Q)$, VE fit result, and fit components, following the legend of panel (a). Panels (c) and (d) show the time correlation and its spectrum, respectively, on a semilogarithmic scale in order to better appreciate the quality of the fit (red-solid curve).

data is less accurate than the VE one, even at our lowest $Q$ value. Note that for an easier comparison with other published data, we used as spectral variable the angular frequency $\omega$ in units of rad ps$^{-1}$.

An example of the results of the VE fits to the FK-QCW $F_K(Q, t)$ is shown in Fig. 11 at the same rather high $Q$ shown for RPMD in Fig. 9. Again, a VE description is found to be appropriate, although the FK-QCW simulations display a more noisy character than the RPMD ones, as can be seen in Fig. 6. Consequently, FK-QCW fits shown in Fig. 11 are of a slightly lower, though still very good, quality than those of the RPMD case. Indeed, such a quality difference can only be appreciated in the semilogarithmic plots of Figs. 11(c) and 11(d).

Thus, our analysis confirms that, notwithstanding the approximations discussed in Sec. V, the $F_K(Q, t)$ obtained from the quantum methods considered here comply with the general property of having a multi-exponential representation, and that a viscoelastic description applies also to liquid $D_2$, in the explored $Q$ range.

In Fig. 12(a) the experimental dispersion curve $\omega_s(Q)$ is compared with the one obtained from the fits to the RPMD and FK-QCW simulations, all curves showing a considerable positive dispersion with respect to the hydrodynamic limit curve, $\omega_{s,\mathrm{hyd}}(Q) = c_s Q$, also shown in the figure. A similar comparison is performed in panel (b) for the damping $z_s(Q)$ and the undamped frequency $\Omega_s(Q) = \sqrt{\omega_s^2(Q) + z_s^2(Q)}$ of the longitudinal excitations. As was evident also from Fig. 6, a larger difference is observed in the damping of the acoustic modes in the whole experimental $Q$ range. By contrast, the frequency $\omega_s(Q)$ deduced from RPMD and FK-QCW only progressively deviates from the experimental one as $Q$ grows, with FK-QCW better accounting for the experimental result. It is important to observe that the error bars of the shown experimental quantities are of the order of the size of the symbols. This means that the excitations, as determined by the fit to the measured data, have very marked features leading to rather small uncertainties. We note that the results for the undamped frequency, from both experiment and simulation, seem to be quite larger than those reported in Fig. 10 of Ref. [24], in Fig. 2 of Ref. [27], and in Fig. 4 of Ref. [28]. For instance, despite the fact that the temperature of the three measurements was nearly the same ($\simeq$20 K), the first paper reports a maximum of $\hbar\Omega_s(Q)$ of about 7 meV, the second paper of 8.5 meV, and the third of 7.5 meV, which are all substantially lower than the current value of $\simeq$10 meV. The three experiments all corresponded to samples with a higher sound speed than ours (implying a slightly larger density), so the origin of the discrepancy is even more difficult to explain.

Concerning the experimental determinations of the damping, all previous estimates provide (around $Q_p/2$) a roughly common value of about 5 meV, despite the different values given instead for $\Omega_s$. However, due to the slightly lower density of our state, such a result is, in principle, not at variance

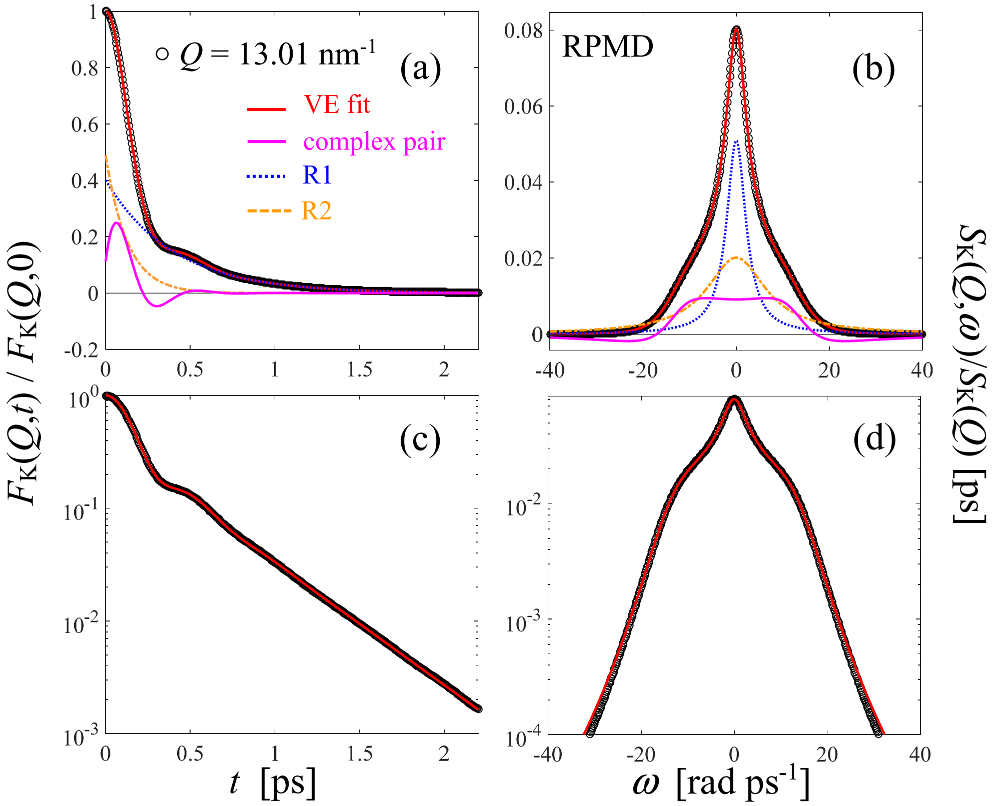

FIG. 9. Same as Fig. 8 at $Q = 13.01$ nm$^{-1}$.

with the current ones from RPMD and FK-QCW (∼4 meV), as well as from the experiment (∼3 meV). In fact, as stated for cold liquids and for normal liquid He [77,78], not only the frequency, but also the damping of sound waves increases as density grows, as it happens for classical fluids. Nevertheless, the above considerations clearly imply that the corresponding dispersion curves $\omega_s(Q)$ would completely differ, i.e., would reach far smaller frequencies at all wave vectors, from those of Fig. 12(a).

The reasons of such differences might lie, of course, in possible, although improbable, experimental problems in present or previous neutron measurements. However, given the very complex analysis of neutron data in the case of liquid $D_2$, one can more likely hypothesize discrepancies due to the neutron data correction procedures. One problem, among others, being the critical evaluation and subtraction of the single-molecule contribution. Indeed, the self component in Fig. 5 of Ref. [24] seems rather unrealistic, given that the experimental resolution was not so different from ours. The same applies to the one reported in Fig. 3 of Ref. [28], in which no fingerprint of the rotational transition around 7 meV is visible, while we clearly showed, in Figs. 2(d) and 5, how

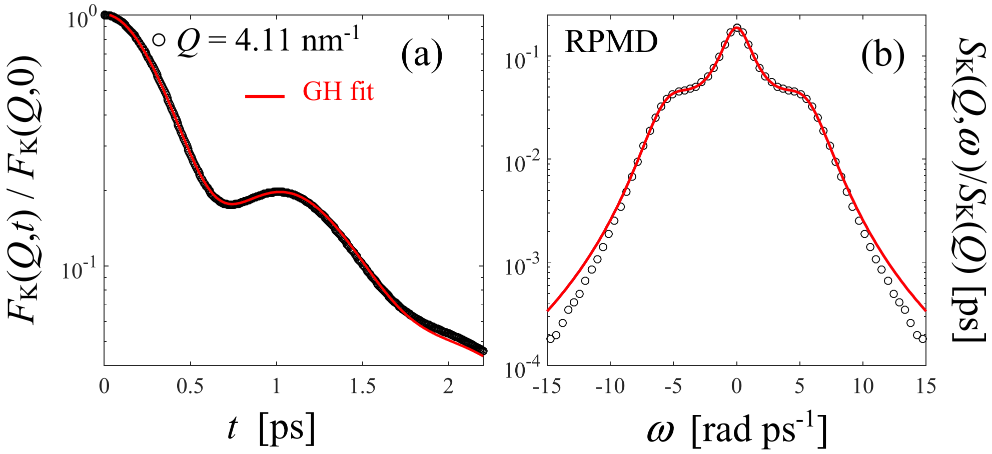

FIG. 10. Same as Figs. 8(c) and 8(d) but in the case of a GH fit to the RPMD data.

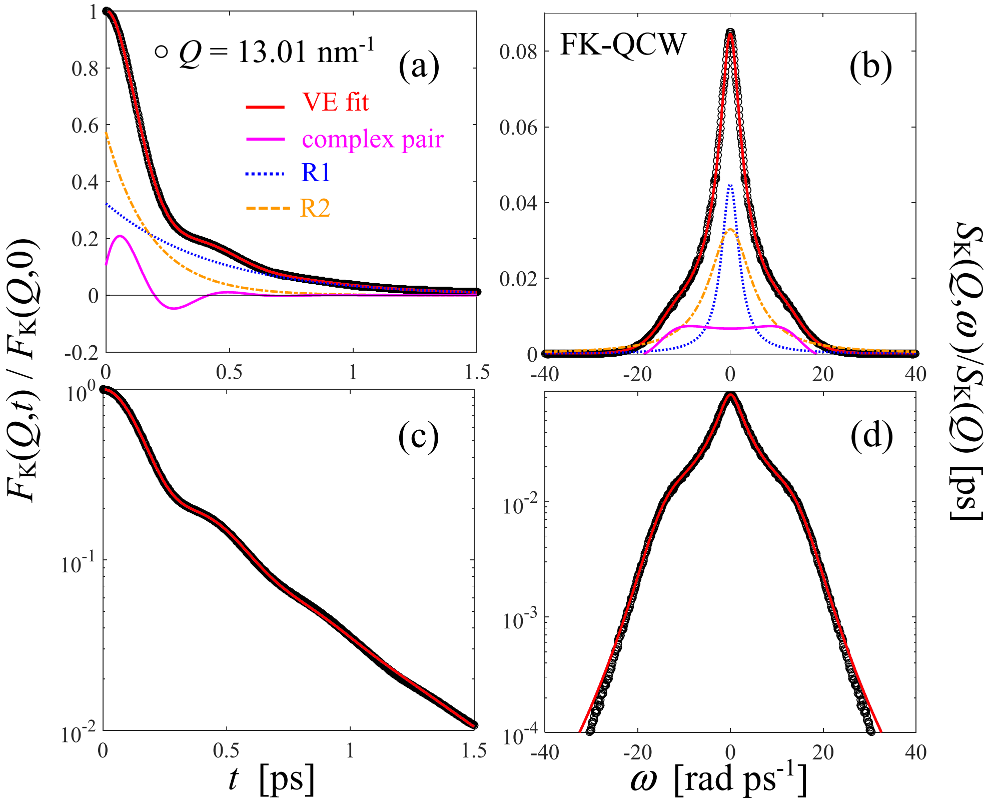

FIG. 11. Same as Fig. 9 but referring to the FK-QCW simulations. Note that the cutoff in time is shorter than in Fig. 9, due to some noise in these results that was absent in the RPMD data. Consequently, also the fit quality, though more than acceptable, is inferior to that of the RPMD case, as it is particularly evident from panels (c) and (d).

much it interferes with the Brillouin peak and, consequently, with the fitted values of both $\omega_s$ and $z_s$. Further, in Ref. [27] the self component was accounted for by assuming the ideal gas $S_s(Q,\omega)$ in the Young and Koppel model, which is not a good approximation for such a critical correction. This can be deduced from Fig. 13, where we show the quite different fit we obtain [to be compared to that of Fig. 2(c)] if the ideal gas lineshape is used in place of the quantum $S_s^{GA}(Q,\omega)$ in the calculation of $J_s(Q,\omega)$. The crucial difference between the two is that the correct quantum asymmetry of the ideal gas is simply due to the frequency shift introduced by recoil. Conversely, the $S_s^{GA}(Q,\omega)$ obeys the first moment sum rule because of its shape, and not through a frequency shift. It is clear then that the subtraction based on these two lineshapes has quite different effects in the two cases. Interestingly, by the fit shown in Fig. 13 we obtain a rather lower value of the undamped frequency (8.2 meV). Another important difference is that in the previous works no mention is made about the imposition of physical constraints, which in this case are a particularly important requirement. Without this condition, the fit is much more flexible and can provide different results, which naturally better adapt to the data points. For instance, an unconstrained fit at $Q = 9$ nm$^{-1}$ in Fig. 3 would have provided a better description of the points on the right wing of the spectrum, but at the cost of having a wrong $M^{(1)}$ and consequently different values for $\omega_s$ and $z_s$.

Finally, in Fig. 14 we show the amplitude [panel (a)] and damping [panel (b)] of the real mode (labelled as $R_0$) obtained from the GH fit to the experimental data. In both panels, these are compared with the corresponding quantities that describe the central part of the RPMD spectra in a VE modeling, i.e., those related to the two central Lorentzians $R_1$ and $R_2$. The comparisons shown in Fig. 14(a) resemble very much the trends already observed in other insulating liquids, like $CO_2$ [79]. However, these are specially interesting as soon as we look at the sum of the intensities of the two real modes of the VE fits to the simulations. Indeed, such a sum is found to nicely agree with the experimental amplitude. This means that the GH model describes rather well, though in an effective way, the more detailed structure of the central peak confirmed by the VE fits to the RPMD data. Moreover, this fact also confirms what we mentioned before, i.e., that the relaxation modes in the liquid are almost equally witnessed by the neutron data and by the RPMD simulations. By contrast, the source of the discrepancies mainly lies in the way propagating excitations appear to be damped.

## VII. CONCLUSIONS

We presented the results of an inelastic neutron scattering experiment aimed at determining the center-of-mass dynamics of liquid $D_2$, that is its characteristic relaxation processes and excitations. For applicative purposes, we were also interested in providing both the dynamic structure factor of this liquid and its neutron DDCS in absolute units. We performed a rather demanding analysis of the neutron data, using

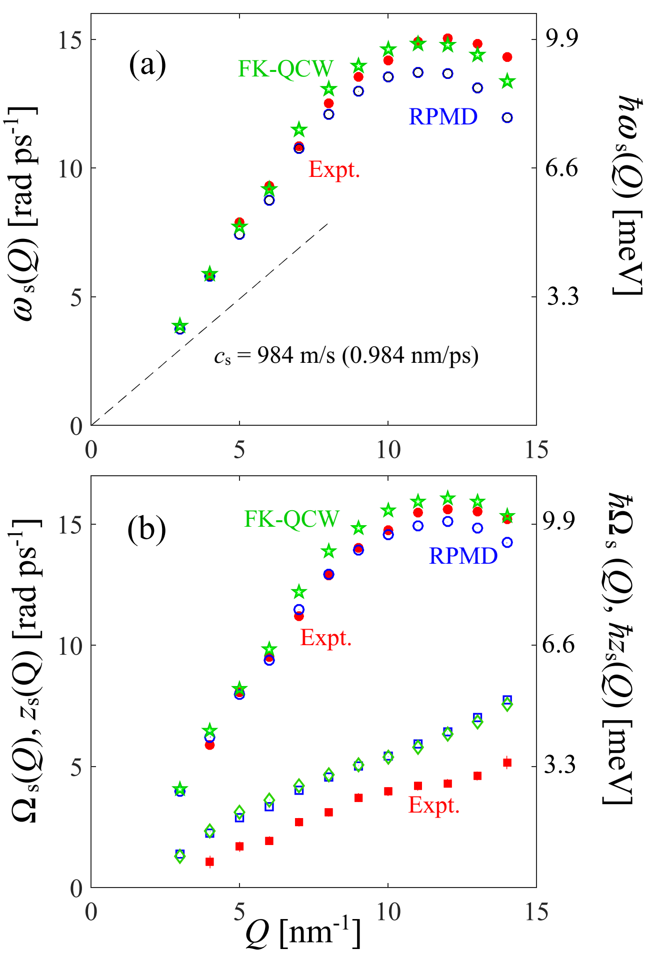

FIG. 12. (a) Experimental (red-full circles), RPMD (blue-empty circles), and FK-QCW (green-empty stars) dispersion curve of the longitudinal modes. The hydrodynamic linear behavior is also shown as a dashed-black line. (b) The RPMD and FK-QCW values for the undamped frequency $\Omega_s(Q)$ are reported with the same symbols used in panel (a). The damping $z_s(Q)$ of the sound modes turns out to nearly coincide in both the FK-QCW (green-empty diamonds) and RPMD (blue empty squares) cases. Full-red symbols are used for the corresponding experimental quantities.

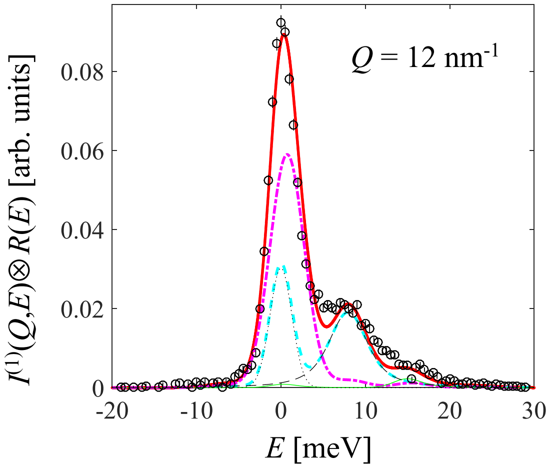

FIG. 13. Same as Fig. 2(c) but using the ideal gas lineshape in the calculation of $J_s(Q,\omega)$ of Eq. (6) (magenta-chain curve).

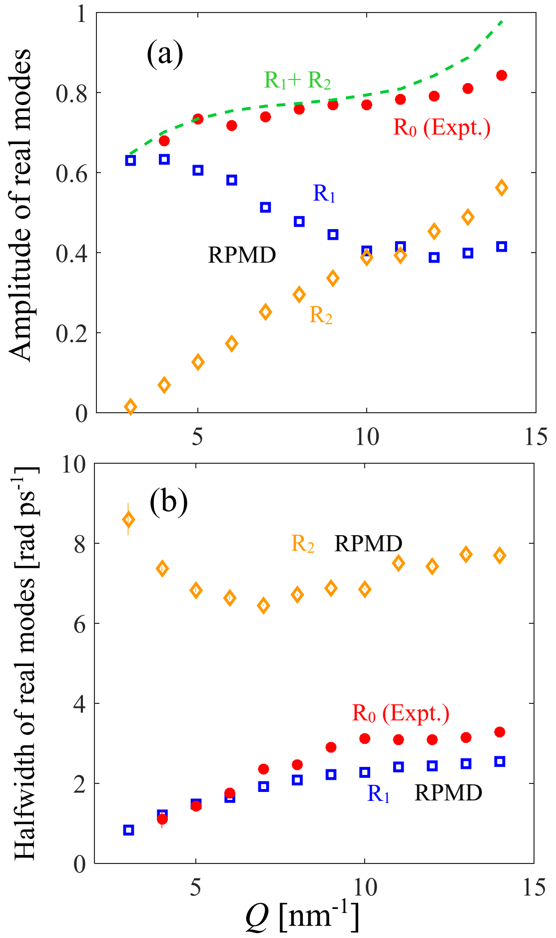

FIG. 14. $Q$ dependence of the amplitudes and dampings of the real modes considered in a GH modeling of the neutron data (labelled as $R_0$, full red circles) and in a VE one of the simulated RPMD spectra, with $R_1$ represented by the blue empty squares, and $R_2$ by orange empty diamonds. In panel (a) the sum of the $R_1$ and $R_2$ VE contributions to the central RPMD spectrum is also compared with the effective one obtained from experiment.

the best available methods at present for the calculation of the single-molecule contribution, which must be subtracted from the total neutron signal to access $S(Q,\omega)$. This step is particularly complex because of the quantum nature of $D_2$, which requires a quantum compliant evaluation of its self dynamic structure factor $S_s(Q,\omega)$ that, as we showed, cannot be crudely substituted by an ideal gas approximation, at least when performing a correction as important as the subtraction of the single-molecule term from the neutron data.

We complemented the experimental part with an extensive simulation work aimed at comparing also different quantum algorithms whose effectiveness for direct calculations of the $S(Q,\omega)$ of a quantum fluid is, actually, still completely unsettled. This is also another reason explaining why we were striving to perform comparisons on an absolute scale and free from experimental or simulation resolution effects. Our work reveals that, when doing so, appreciable discrepancies emerge not only between experiment and all the attemped simulation algorithms (RPMD, FK-LPI, FK-QCW), but also among the different simulation methods. As clearly stated in this work, it is evident that something in the algorithms deeply affects the way longitudinal acoustic modes are described. This point regarding different simulation techniques should indeed be the objective of future investigations and simulation research. As far as the disagreement between simulations and experiment is concerned, of course we cannot exclude experimental problems due to possible systematic errors. Anyway, as stated before, we performed a very careful analysis that also took advantage of the unique opportunity, provided by the multi-exponential expansion of correlation functions, of easily imposing physical constraints in fit procedures. In fact, our comparisons show that important details of the spectral shape might be missed either by experiment or by calculations or both, but the absolute scale of the functions is correct in either way. This hopefully means that the main thing to understand further is why simulation data have so less marked collective sound excitations with respect to the present experimental results for $S(Q, \omega)$.

It is well known that cold liquids [77,80], and He in particular [81], are characterized by rather long lifetimes (ideally infinite in superfluid He) of the collective excitations, with respect to classical liquids. This behavior was interpreted as the main manifestation, in the dynamical properties, of the quantum nature of such fluids [80,81]. To what extent also liquid $D_2$ might show so clear dynamical evidences of quantum effects it is difficult to say. Our experimental results seem to suggest that quantum delocalization visibly affects the damping of propagating modes in liquid $D_2$, even more than RPMD and the other simulation techniques are able to predict. Although, for brevity, we classified as “quantum” the considered simulation methods, it is important to recall that, unavoidably, they are all the result of semi-classical approximations, which might be unable to fully grasp the most typical fingerprint in $S(Q, \omega)$ of genuine quantum behavior.

Finally, still concerning our dynamical characterization of liquid $D_2$, both by VE fits to RPMD/FK-QCW data, and by GH fits to the neutron ones, we do not observe striking differences from the behavior of other insulating liquids [79], also showing a marked positive dispersion as liquid $D_2$. The overall acceptable agreement of the RPMD/FK-QCW and experimental dispersion curves, indeed confirms that the most studied property in liquids dynamics is reasonably captured by both our experiment and simulations on liquid $D_2$.

## ACKNOWLEDGMENTS

The authors wish to thank the ILL staff, and particularly Simon Baudoin, for the invaluable support during the experiment, ensuring security aspects, and a total control on the preparation of a nonstandard sample as liquid $D_2$. We are also greatly indebted to Walter Penits for technical support of the simulations and numerous discussions about the FK methods. This research was funded by Ministero dell’Istruzione dell’Università e della Ricerca Italiano (Grant No. PRIN2017-2017Z55KCW).

---

[1] S. Bellissima, M. Neumann, U. Bafile, D. Colognesi, F. Barocchi, and E. Guarini, Density and time scaling effects on the velocity autocorrelation function of quantum and classical dense fluid parahydrogen, J. Chem. Phys. **150**, 074502 (2019).

[2] J. P. Hansen and I. R. McDonald, *Theory of Simple Liquids*, 2nd ed. (Academic Press, London, 1986).

[3] W. Marshall and S. Lovesey, *Theory of Thermal Neutron Scattering* (Clarendon Press, Oxford, 1971).

[4] V. F. Sears, Neutron scattering lengths and cross sections, Neutron News **3**, 26 (1992).

[5] R. MacFarlane and D. W. Muir, The NJOY Nuclear Data Processing System, report No. LA-12470-M, Los Alamos National Laboratory, USA, 1994 (unpublished).

[6] D. W. Muir, R. M. Boicourt, and A. C. Kahler, Report No. LAUR-12-27079, Los Alamos National Laboratory, USA, 2012 (unpublished).

[7] N. Morishima and D. Mizobuchi, Cross section models for cold neutron scattering from liquid hydrogen and liquid deuterium, Nucl. Instrum. Methods Phys. Res. A **350**, 275 (1994).

[8] J. R. Granada, V. H. Gillette, M. E. Pepe, and M. M. Sbaffoni, Improved thermal neutron scattering kernels for liquid hydrogen and deuterium, J. Neutr. Res. **11**, 25 (2003).

[9] N. Morishima and Y. Nishikawa, Cold and thermal neutron scattering cross sections of liquid $H_2$ and $D_2$. II: Improvement on coherent scattering, Ann. Nucl. Energy **31**, 737 (2004).

[10] E. Guarini, M. Neumann, U. Bafile, M. Celli, D. Colognesi, E. Farhi, and Y. Calzavara, Velocity autocorrelation in liquid parahydrogen by quantum simulations for direct parameter-free computations of neutron cross sections, Phys. Rev. B **92**, 104303 (2015).

[11] E. Guarini, M. Neumann, U. Bafile, M. Celli, D. Colognesi, S. Bellissima, E. Farhi, and Y. Calzavara, Velocity autocorrelation by quantum simulations for direct parameter-free computations of the neutron cross sections. II. Liquid deuterium, Phys. Rev. B **93**, 224302 (2016).

[12] J. Cao and G. A. Voth, The formulation of quantum statistical mechanics based on the Feynman path centroid density. II. Dynamical properties, J. Chem. Phys. **100**, 5106 (1994).

[13] S. Jang and G. A. Voth, Path integral centroid variables and the formulation of their exact real time dynamics, J. Chem. Phys. **111**, 2357 (1999).

[14] S. Jang and G. A. Voth, A derivation of centroid molecular dynamics and other approximate time evolution methods for path integral centroid variables, J. Chem. Phys. **111**, 2371 (1999).

[15] T. D. Hone and G. A. Voth, A centroid molecular dynamics study of liquid para-hydrogen and ortho-deuterium, J. Chem. Phys. **121**, 6412 (2004).

[16] I. R. Craig and D. E. Manolopoulos, Quantum statistics and classical mechanics: Real time correlation functions from ring polymer molecular dynamics, J. Chem. Phys. **121**, 3368 (2004).

[17] T. F. Miller III and D. E. Manolopoulos, Quantum diffusion in liquid para-hydrogen from ring-polymer molecular dynamics, J. Chem. Phys. **122**, 184503 (2005).

[18] S. Habershon, D. E. Manolopoulos, T. E. Markland, and T. F. Miller III, Ring-polymer molecular dynamics: Quantum effects

in chemical dynamics from classical trajectories in an extended phase space, Annu. Rev. Phys. Chem. **64**, 387 (2013).

[19] I. F. Silvera and V. V. Goldman, The isotropic intermolecular potential for $H_2$ and $D_2$ in the solid and gas phases, J. Chem. Phys. **69**, 4209 (1978).

[20] G. H. Vineyard, Scattering of slow neutrons by a liquid, Phys. Rev. **110**, 999 (1958).

[21] A. Rahman, K. S. Singwi, and A. Sjölander, Theory of Slow Neutron Scattering by Liquids. I, Phys. Rev. **126**, 986 (1962).

[22] E. Guarini, The neutron cross section of the hydrogen liquids: Substantial improvements and perspectives, arXiv:2104.05004.

[23] F. J. Bermejo, J. L. Martínez, D. Martín-Marero, F. J. Mompeán, M. García-Hernández, A. Chahid, G. Senger, and M. L. Ristig, Coherent excitations in liquid deuterium, Physica B: Condens. Matter **180-181**, 845 (1992).

[24] F. J. Bermejo, F. J. Mompeán, M. García-Hernández, J. L. Martínez, D. Martin-Marero, A. Chahid, G. Senger, and M. L. Ristig, Collective excitations in liquid deuterium: Neutron-scattering and correlated-density-matrix results, Phys. Rev. B **47**, 15097 (1993).

[25] F. J. Mompeán, F. J. Bermejo, M. García-Hernández, B. Fåk, J. L. Martínez, G. Senger, and M. L. Ristig, Temperature dependence of collective excitations in liquid deuterium by neutron inelastic scattering, J. Phys.: Condens. Matter **5**, 5743 (1993).

[26] F. J. Mompeán, D. Martín-Marero, M. García-Hernández, F. J. Bermejo, B. Fåk, J. L. Martínez, G. Senger, and M. L. Ristig, Collective excitations in liquid deuterium in three thermodynamic states, J. Mol. Struct. **296**, 313 (1993).

[27] M. Mukherjee, F. J. Bermejo, B. Fåk, and S. M. Bennington, Microscopic dynamics in liquid deuterium: A transition from collective to single-particle regimes, Europhys. Lett. **40**, 153 (1997).

[28] C. Mondelli, M. A. González, F. Albergamo, C. Carbajo, M. J. Torralvo, E. Enciso, F. J. Bermejo, R. Fernández-Perea, C. Cabrillo, V. Leon, and M. L. Saboungi, Collective excitations in liquid $D_2$ confined within the mesoscopic pores of a MCM-41 molecular sieve, Phys. Rev. B **73**, 094206 (2006).

[29] A. Cunsolo, D. Colognesi, M. Sampoli, R. Senesi, and R. Verbeni, Signatures of quantum behavior in the microscopic dynamics of liquid hydrogen and deuterium, J. Chem. Phys. **123**, 114509 (2005).

[30] J. A. Poulsen, G. Nyman, and P. J. Rossky, Practical evaluation of condensed phase quantum correlation functions: A Feynman–Kleinert variational linearized path integral method, J. Chem. Phys. **119**, 12179 (2003).

[31] K. K. G. Smith, J. A. Poulsen, A. Cunsolo, and P. J. Rossky, Refinement of the experimental dynamic structure factor for liquid parahydrogen and orthodeuterium using semi-classical quantum simulation, J. Chem. Phys. **140**, 034501 (2014).

[32] K. K. G. Smith, J. A. Poulsen, G. Nyman, A. Cunsolo, and P. J. Rossky, Application of a new ensemble conserving quantum dynamics simulation algorithm to liquid para-hydrogen and ortho-deuterium, J. Chem. Phys. **142**, 244113 (2015).

[33] K. K. G. Smith, J. A. Poulsen, G. Nyman, and P. J. Rossky, A new class of ensemble conserving algorithms for approximate quantum dynamics: Theoretical formulation and model problems, J. Chem. Phys. **142**, 244112 (2015).

[34] F. Barocchi, U. Bafile, and M. Sampoli, Exact exponential function solution of the generalized Langevin equation for autocorrelation functions of many-body systems, Phys. Rev. E **85**, 022102 (2012).

[35] F. Barocchi and U. Bafile, Expansion in Lorentzian functions of spectra of quantum autocorrelations, Phys. Rev. E **87**, 062133 (2013).

[36] F. Barocchi, E. Guarini, and U. Bafile, Exponential series expansion for correlation functions of many-body systems, Phys. Rev. E **90**, 032106 (2014).

[37] V. F. Sears, Theory of cold neutron scattering by homonuclear diatomic liquids. I. Free rotation, Can. J. Phys. **44**, 1279 (1966).

[38] E. Guarini, The neutron double differential cross-section of simple molecular fluids: Refined computing models and nowadays applications, J. Phys.: Condens. Matter **15**, R775 (2003).

[39] J. A. Young and J. U. Koppel, Slow neutron scattering by molecular hydrogen and deuterium, Phys. Rev. **135**, A603 (1964).

[40] D. M. Ceperley, Path integrals in the theory of condensed helium, Rev. Mod. Phys. **67**, 279 (1995).

[41] R. Kubo, The fluctuation-dissipation theorem, Rep. Prog. Phys. **29**, 255 (1966).

[42] U. Balucani and M. Zoppi, *Dynamics of the Liquid State* (Clarendon Press, Oxford, 1994).

[43] E. Guarini *et al.*, Dynamics of liquid para-hydrogen: A low-Q determination of its double differential cross section, Institut Laue-Langevin (ILL) doi:10.5291/ILL-DATA.6-02-551; Concerning the title of the experiment, explanations can be found in the Experimental Report downloadable at http://doi.ill.fr/10.5291/ILL-DATA.6-02-551.

[44] D. Aisa, E. Babucci, F. Barocchi, A. Cunsolo, F. D. 'Anca, A. D. Francesco, F. Formisano, T. Gahl, E. Guarini, S. Jahn *et al.*, The development of the BRISP spectrometer at the Institut Laue-Langevin, Nucl. Instrum. Methods Phys. Res. A **544**, 620 (2005).

[45] D. Aisa, S. Aisa, E. Babucci, F. Barocchi, A. Cunsolo, A. De Francesco, F. Formisano, T. Gahl, E. Guarini, A. Laloni *et al.*, BRISP: A new thermal-neutron spectrometer for small-angle studies of disordered matter, J. Non-Cryst. Solids **352**, 5130 (2006).

[46] F. Formisano, E. Guarini, A. Laloni, A. Orecchini, C. Petrillo, W. C. Pilgrim, D. Russo, and F. Sacchetti, The neutron spectrometer BRISP: A new approach to the study of excitations in condensed matter at low momentum transfer in the milli-eV energy region, J. Phys. Soc. Jpn. **82**, SA028 (2013).

[47] M. Zoppi, U. Bafile, E. Guarini, F. Barocchi, R. Magli, and M. Neumann, Microscopic Structure and Intermolecular Potential in Liquid Deuterium, Phys. Rev. Lett. **75**, 1779 (1995).

[48] E. W. Lemmon, M. O. McLinden, and D. G. Friend, *Thermophysical Properties of Fluid Systems*, NIST Chemistry WebBook, NIST Standard Reference Database No. 69, edited by P. J. Linstrom and W. G. Mallard (National Institute of Standards and Technology, Gaithersburg, MD, 2017), Available at http://webbook.nist.gov.

[49] E. Guarini, U. Bafile, F. Barocchi, A. De Francesco, E. Farhi, F. Formisano, A. Laloni, A. Orecchini, A. Polidori, M. Puglini, and F. Sacchetti, Dynamics of liquid Au from neutron Brillouin scattering and *ab initio* simulations: Analogies in the behavior of metallic and insulating liquids, Phys. Rev. B **88**, 104201 (2013).

[50] E. Guarini, A. De Francesco, U. Bafile, A. Laloni, B.G. delRio, D. J. Gonzalez, L. E. Gonzalez, F. Barocchi, and F. Formisano, Neutron Brillouin scattering and *ab initio* simulation study of

the collective dynamics of liquid silver, Phys. Rev. B **102**, 054210 (2020).

[51] D. Richard, M. Ferrand, and G. J. Kearley, Analysis and visualisation of neutron-scattering data, J. Neutron Research **4**, 33 (1996).

[52] Instructions for the use of LAMP can be found at https://www.ill.eu/users/support-labs-infrastructure/software-scientific-tools/lamp/.

[53] A. De Francesco, U. Bafile, F. Formisano, and E. Guarini, Efficient implementation of multiple scattering Monte Carlo estimates in time-of-flight neutron spectrometry exploiting wide-area detectors, J. Phys.: Conf. Ser. **340**, 012024 (2012).

[54] K. Sköld, Small Energy Transfer Scattering of Cold Neutrons from Liquid Argon, Phys. Rev. Lett. **19**, 1023 (1967).

[55] E. Guarini, S. Bellissima, U. Bafile, E. Farhi, A. De Francesco, F. Formisano, and F. Barocchi, Density of states from mode expansion of the self-dynamic structure factor of a liquid metal, Phys. Rev. E **95**, 012141 (2017).

[56] E. Guarini, M. Neumann, U. Bafile, S. Bellissima, and D. Colognesi, Dynamical Origin of the Total and Zero-Point Kinetic Energy in a Quantum Fluid, Phys. Rev. Lett. **123**, 135301 (2019).

[57] E. Guarini, M. Neumann, S. Bellissima, D. Colognesi, and U. Bafile, Density dependence of the dynamical processes governing the velocity autocorrelation function of a quantum fluid, Phys. Rev. E **100**, 062111 (2019).

[58] U. Bafile, M. Neumann, D. Colognesi, and E. Guarini, Time dependence of quantum correlation functions, Phys. Rev. E **101**, 052110 (2020).

[59] U. Bafile, E. Guarini, and F. Barocchi, Collective acoustic modes as renormalized damped oscillators: Unified description of neutron and x-ray scattering data from classical fluids, Phys. Rev. E **73**, 061203 (2006).

[60] I. M. de Schepper, P. Verkerk, A. A. van Well, and L. A. de Graaf, Short-Wavelength Sound Modes in Liquid Argon, Phys. Rev. Lett. **50**, 974 (1983).

[61] I. M. de Schepper, J. C. van Rijs, A. A. van Well, P. Verkerk, and L. A. de Graaf, Microscopic sound waves in dense Lennard-Jones fluids, Phys. Rev. A **29**, 1602 (1984).

[62] M. Ceriotti, M. Parrinello, Th. E. Markland, and D. E. Manolopoulos, Efficient stochastic thermostatting of path integral molecular dynamics, J. Chem. Phys. **133**, 124104 (2010).

[63] G. Bussi, D. Donadio, and M. Parrinello, Canonical sampling through velocity rescaling, J. Chem. Phys. **126**, 014101 (2007).

[64] I. R. Craig and D. E. Manolopoulos, Inelastic neutron scattering from liquid para-hydrogen by ring polymer molecular dynamics, Chem. Phys. **322**, 236 (2006).

[65] J. A. Poulsen, G. Nyman, and P. J. Rossky, Determination of the Van Hove spectrum of liquid He(4): An application of the Feynman–Kleinert linearized path integral methodology, J. Phys. Chem. A **108**, 8743 (2004).

[66] J. A. Poulsen, G. Nyman, and P. J. Rossky, Quantum diffusion in liquid para-hydrogen: An application of the Feynman–Kleinert linearized path integral approximation, J. Phys. Chem. B **108**, 19799 (2004).

[67] J. A. Poulsen, G. Nyman, and P. J. Rossky, Feynman–Kleinert linearized path integral (FK-LPI) algorithms for quantum molecular dynamics, with application to water and He(4), J. Chem. Theory Comput. **2**, 1482 (2006).

[68] J. A. Poulsen, J. Scheers, G. Nyman, and P. J. Rossky, Quantum density fluctuations in liquid neon from linearized path-integral calculations, Phys. Rev. B **75**, 224505 (2007).

[69] This is the generalization of Eq. (43) of Ref. [65] to arbitrary wave vectors $\boldsymbol{Q} = (Q_x, Q_y, Q_z)$.

[70] E. Anderson, Z. Bai, C. Bischof, S. Blackford, J. Demmel, J. Dongarra, J. Du Croz, A. Greenbaum, S. Hammarling, A. McKenney, and D. Sorensen, *LAPACK Users' Guide*, 3rd edition (Society for Industrial and Applied Mathematics, Philadelphia, 1999). See http://www.netlib.org/lapack.

[71] M. P. Allen and D. J. Tildesley, *Computer Simulation of Liquids* (Clarendon Press, Oxford, 1987).

[72] Specifically, version FK-QCW(2) of Ref. [33].

[73] Note that this does not sample exactly the same distribution as FK-LPI, since $W_1$ contains additional terms.

[74] Since Refs. [32,33] are not very specific in this case, we have chosen to put $f_n(\boldsymbol{q}_c) = 0$ for imaginary frequencies.

[75] In order to limit the length of the paper we show the absolute scale and resolution free DDCS and $S(Q, \omega)$ only at three example $Q$ values. Needless to say, the data at all the experimental wave vectors are available on request, e.g. for possible use in cold source design.

[76] This cutoff in time is usually identified with the time it takes a density fluctuation to propagate over a distance equal to the box length, traveling at the sound speed $c_s$. For a cubic box, it can be evaluated as $t_R = (N/n)^{1/3}/c_s$, with $N$ denoting the number of particles actually considered in the simulations.

[77] W. Montfrooij and I. de Schepper, *Excitations in Simple Liquids, Liquid Metals and Superfluids* (Oxford University Press, New York, 2010).

[78] W. Montfrooij, E. C. Svensson, I. M. de Schepper, and E. G. D. Cohen, Effective eigenmode description of normal and superfluid $^4$He, J. Low Temp. Phys. **109**, 577 (1997).

[79] M. Sampoli, U. Bafile, E. Guarini, and F. Barocchi, Collective dynamics and molecular interactions in liquid CO$_2$ by inelastic neutron scattering and computer simulations, Phys. Rev. B **79**, 214203 (2009).

[80] F. J. Bermejo, K. Kinugawa, C. Cabrillo, S. M. Bennington, B. Fak, M. T. Fernandez-Diaz, P. Verkerk, J. Dawidowski, and R. Fernandez-Perea, Quantum Effects on Liquid Dynamics as Evidenced by the Presence of Well-Defined Collective Excitations in Liquid Para-Hydrogen, Phys. Rev. Lett. **84**, 5359 (2000).

[81] H. H. Glyde, *Excitations in Liquid and Solid Helium* (Clarendon Press, Oxford, 1995).